

ARMY RESEARCH LABORATORY



An Approximate Method for Pitch-Damping Prediction

by James E. Danberg and Paul Weinacht

ARL-TR-3007

July 2003

Approved for public release; distribution is unlimited.

20030917 059

NOTICES

Disclaimers

The findings in this report are not to be construed as an official Department of the Army position unless so designated by other authorized documents.

Citation of manufacturer's or trade names does not constitute an official endorsement or approval of the use thereof.

Destroy this report when it is no longer needed. Do not return it to the originator.

Army Research Laboratory

Aberdeen Proving Ground, MD 21005-5066

ARL-TR-3007

July 2003

An Approximate Method for Pitch-Damping Prediction

James E. Danberg and Paul Weinacht
Weapons and Materials Research Directorate, ARL

Report Documentation Page			<i>Form Approved</i> OMB No. 0704-0188	
<small>Public reporting burden for this collection of information is estimated to average 1 hour per response, including the time for reviewing instructions, searching existing data sources, gathering and maintaining the data needed, and completing and reviewing the collection information. Send comments regarding this burden estimate or any other aspect of this collection of information, including suggestions for reducing the burden, to Department of Defense, Washington Headquarters Services, Directorate for Information Operations and Reports (0704-0188), 1215 Jefferson Davis Highway, Suite 1204, Arlington, VA 22202-4302. Respondents should be aware that notwithstanding any other provision of law, no person shall be subject to any penalty for failing to comply with a collection of information if it does not display a currently valid OMB control number.</small> PLEASE DO NOT RETURN YOUR FORM TO THE ABOVE ADDRESS.				
1. REPORT DATE (DD-MM-YYYY) July 2003		2. REPORT TYPE Final		3. DATES COVERED (From - To) 2002-2003
4. TITLE AND SUBTITLE An Approximate Method for Pitch-Damping Prediction			5a. CONTRACT NUMBER	
			5b. GRANT NUMBER	
			5c. PROGRAM ELEMENT NUMBER	
6. AUTHOR(S) James E. Danberg and Paul Weinacht			5d. PROJECT NUMBER 1L1612618AH80	
			5e. TASK NUMBER	
			5f. WORK UNIT NUMBER	
7. PERFORMING ORGANIZATION NAME(S) AND ADDRESS(ES) U.S. Army Research Laboratory ATTN: AMSRL-WM-BC Aberdeen Proving Ground, MD 21005-5066			8. PERFORMING ORGANIZATION REPORT NUMBER ARL-TR-3007	
9. SPONSORING/MONITORING AGENCY NAME(S) AND ADDRESS(ES)			10. SPONSOR/MONITOR'S ACRONYM(S)	
			11. SPONSOR/MONITOR'S REPORT NUMBER(S)	
12. DISTRIBUTION/AVAILABILITY STATEMENT Approved for public release; distribution is unlimited.				
13. SUPPLEMENTARY NOTES				
14. ABSTRACT A simple method of estimating the pitch-damping coefficients for axisymmetric flight bodies has been developed. The method is suitable for preliminary design and parametric studies. The procedure is based on concepts from slender body theory, but the method significantly improves the accuracy of the results through the use of correlation functions. To derive the correlation functions, extensive use of a recently developed and validated computational fluid dynamics (CFD) method for predicting the pitch-damping coefficients has been employed. The CFD method provides important details necessary to derive the correlation functions that are unavailable from the current experimental database. The method has been validated for a variety of nose geometries, body lengths, and Mach numbers using both experimental and computationally generated databases.				
15. SUBJECT TERMS computational fluid dynamics, projectile aerodynamics, flight mechanics				
16. SECURITY CLASSIFICATION OF:			17. LIMITATION OF ABSTRACT UL	18. NUMBER OF PAGES 42
a. REPORT UNCLASSIFIED	b. ABSTRACT UNCLASSIFIED	c. THIS PAGE UNCLASSIFIED		
				19b. TELEPHONE NUMBER (Include area code) 410-278-4280

Contents

List of Figures	iv
List of Tables	v
1. Introduction	1
1.1 Slender Body Theory Relationships.....	2
1.2 Relationships Between Coefficients.....	4
2. Formulation of an Approximate Model	9
2.1 $G(x)$ on Cylinder (Carry-Over Transformation)	10
2.2 Effect of Nose Length	14
2.3 Correlation for the Nose Region	15
2.4 Pitch Damping Force, C_{Nq} (Sacks's Relationship).....	16
2.5 Pitch-Damping Moment Coefficient Sum.....	17
2.6 Reynolds Number Effects	19
3. Application of the Approximate Model	20
4. Conclusion	30
5. References	32
List of Abbreviations	34

List of Figures

Figure 1. Schematic of ANSR rocket configuration.....	2
Figure 2. Comparison of predicted normal force coefficient slope $C_{N\alpha}$ distribution with slender body theory for the ANSR.....	5
Figure 3. Comparison of PNS and slender body theory predictions of pitch-damping force coefficients over body, ANSR, Mach 2.5, $X_{cg}/D = 5.038$	5
Figure 4. Comparison of pitch-damping force coefficient $C_{N\dot{\alpha}}$ with integral of normal force coefficient over body, Mach 2.5, ANSR, CFD predictions.....	8
Figure 5. Comparison between C_{Nq} and $C_{N\dot{\alpha}} - C_{m\dot{\alpha}}$ (equation 11), Mach 2.5, ANSR, $X_{cg}/D = 5.038$, CFD predictions.....	9
Figure 6. $G(x)$ over the ANSR for various Mach numbers.....	10
Figure 7. Correlation of $G(x)$ on the cylindrical afterbody, ANSR.	11
Figure 8. Similarity factors $S(M)$ and $T(M)$	13
Figure 9. Correlation of $G_{25}(X_{25})$ with computed data, ANSR.....	13
Figure 10. Effect of nose length on $G(x)$, tangent-ogive/cylinder, Mach 2.5.....	14
Figure 11. Variation of $G(\text{nose})$ with Mach number and cone angle for conical noses.	15
Figure 12. Distribution of $H(x)$ along body for ANSR.....	17
Figure 13. Comparison of PNS and approximate method predictions of pitch-damping force coefficients over body, ANSR, Mach 2.5, $X_{cg}/D = 5.038$	18
Figure 14. Comparison of PNS and approximate method predictions of pitch-damping moment coefficients over body, ANSR, Mach 2.5, $X_{cg}/D = 5.038$	18
Figure 15. Comparison of slender body theory, PNS, and approximate method predictions of pitch-damping moment coefficient sum over body, ANSR, Mach 2.5, $X_{cg}/D = 5.038$	20
Figure 16. Correlation between approximate method predictions and experimental data for $C_{mq} + C_{m\dot{\alpha}}$, ANSR, $L/D = 5, 7$, and 9 , and Mach $1.3, 1.8$, and 2.5	21
Figure 17. Correlation between approximate method predictions and CFD computations for $C_{mq} + C_{m\dot{\alpha}}$, ANSR, $L/D = 5, 7$, and 9 , and Mach $1.3, 1.8$, and 2.5	22
Figure 18. Correlation between approximate method predictions and CFD computations for $C_{mq} + C_{m\dot{\alpha}}$, cone cylinder and tangent ogive cylinder bodies, $L/D = 5, 7$, and 9	23
Figure 19. Correlation between approximate method predictions and CFD computations for $C_{mq} + C_{m\dot{\alpha}}$, cone cylinder and tangent ogive cylinder bodies, $L/D = 12, 15$, and 20	24

Figure 20. Correlation between approximate method predictions and CFD computations for $C_{m\dot{\alpha}}$, cone cylinder and tangent ogive cylinder bodies, $L/D = 5, 7$, and 9 .	24
Figure 21. Correlation between approximate method predictions and CFD computations for $C_{m\dot{\alpha}}$, cone cylinder and tangent ogive cylinder bodies, $L/D = 12, 15$, and 20 .	25
Figure 22. Correlation between approximate method predictions and CFD computations for C_{mq} , cone cylinder and tangent ogive cylinder bodies, $L/D = 5, 7$, and 9 .	25
Figure 23. Correlation between approximate method predictions and CFD computations for C_{mq} , cone cylinder and tangent ogive cylinder bodies, $L/D = 12, 15$, and 20 .	26
Figure 24. Comparison of predicted Mach number variation of $C_{mq} + C_{m\dot{\alpha}}$ obtained from approximate method and CFD computations, cone cylinder bodies, $L_{nose}/D = 2$, $L/D = 5$, 7 , and 9 .	27
Figure 25. Comparison of predicted Mach number variation of $C_{mq} + C_{m\dot{\alpha}}$ obtained from approximate method and CFD computations, tangent ogive cylinder bodies, $L_{nose}/D = 2$, $L/D = 5, 7$, and 9 .	27
Figure 26. Comparison of predicted Mach number variation of $C_{mq} + C_{m\dot{\alpha}}$ obtained from approximate method and CFD computations, cone cylinder bodies, $L_{nose}/D = 2$, $L/D = 12, 15$, and 20 .	28
Figure 27. Comparison of predicted Mach number variation of $C_{mq} + C_{m\dot{\alpha}}$ obtained from approximate method and CFD computations, tangent ogive cylinder bodies, $L_{nose}/D = 2$, $L/D = 12, 15$, and 20 .	28
Figure 28. Comparison of predicted effect of nose length on $C_{mq} + C_{m\dot{\alpha}}$ obtained from approximate method and CFD computations, tangent ogive cylinder bodies, $L/D = 7$.	29
Figure 29. Comparison of predicted effect of nose length on $C_{mq} + C_{m\dot{\alpha}}$ obtained from approximate method and CFD computations, cone cylinder bodies, $L/D = 7$.	30

List of Tables

Table 1. G_{25} as a function of X_{25} .	12
Table 2. Coefficients of the fifth-order polynomial fit of equation 27.	16
Table 3. Center of gravity locations as a function of body length.	23

INTENTIONALLY LEFT BLANK.

1. Introduction

Computational fluid dynamics (CFD) has been shown to provide accurate predictions of the pitch-damping coefficients for a variety of projectile and missile geometries (1-6). In addition to the global coefficients for the complete configuration, the CFD results allow important details, such as the distribution of the force and moment along the body, to be examined. These details would be difficult to investigate experimentally. For some preliminary design and parametric studies, it may be convenient to have a simpler way of estimating the pitch-damping characteristics of flight bodies. Such models do currently exist (7-9), although they are currently being reexamined and updated (10, 11), in part, due to the recent availability of computationally derived pitch-damping data. This report documents the development of an engineering model for predicting the pitch-damping characteristics of axisymmetric flight bodies in supersonic flow. The engineering model is based, in part, on slender body theory and some of the relationships between the aerodynamic coefficients that can be derived from it.

There are two primary pitch-damping force coefficients, C_{N_q} and $C_{N_{\dot{\alpha}}}$, that account for forces produced by the angular rate of the body q and angular rate $\dot{\alpha}$ associated with the angle of attack. For rectilinear flight, the angular rate of the body and the angular rate due to angle of attack are closely related. In this case, the aerodynamic effect represented by the individual coefficients C_{N_q} and $C_{N_{\dot{\alpha}}}$ can be combined and treated as a single coefficient, the pitch-damping force coefficient sum, $C_{N_q} + C_{N_{\dot{\alpha}}}$. Despite this simplification, the individual pitch-damping coefficients may still be required for some aerodynamic analyses. It is therefore desirable to develop a method of predicting the individual pitch-damping coefficients from which the pitch-damping coefficient sum can be easily computed. In most cases, the pitch-damping moment coefficients, C_{m_q} , $C_{m_{\dot{\alpha}}}$, and $C_{m_q} + C_{m_{\dot{\alpha}}}$ are of primary interest because of their importance to the aerodynamic damping. However, these coefficients are easily obtained once the corresponding force coefficients are determined.

By applying slender body theory, it becomes apparent that the pitch-damping force coefficient due to rate of angle of attack change, $C_{N_{\dot{\alpha}}}$, is of primary importance because of its relationship to the normal force and all the other damping coefficients. Correlation functions that are evaluated from CFD computation are introduced into the slender body theory equation for $C_{N_{\dot{\alpha}}}$ to form the basis for an engineering model to estimate the pitch-damping coefficients for axisymmetric bodies. The model is then applied to a variety of axisymmetric body geometries over a range of supersonic Mach numbers, and comparisons are made with CFD predictions for the same body geometries to evaluate the effectiveness of the correlation functions.

An extensive database of pitch-damping coefficient data for a variety of axisymmetric body geometries and flight conditions was generated using results from a recently developed computational procedure for predicting the static and pitch-damping coefficients (1–3). The technique makes use of a novel rotating coordinate frame to compute the aerodynamics associated with the various pitch-damping coefficients. The technique has been embodied into several codes including a Parabolized Navier-Stokes (PNS) technique (1–3) and time-marching Navier-Stokes approach (F3D) (4). The original studies focused on the Army-Navy Spinner Rocket (ANSR) shown in Figure 1. High quality aerodynamic range data were used to validate the computational procedure. For the current study, the database has been expanded to include additional Mach numbers (Mach 1.8–4.5) and longer body lengths (up to length-to-diameter ratio $[L/D] = 20$) as well as a variety of nose geometries. An important feature of the computational data is that the distribution of the aerodynamic forces and moments along the body due to both the static and dynamic aerodynamic coefficients is obtained. It is unlikely that this type of data could be obtained from experimental means.

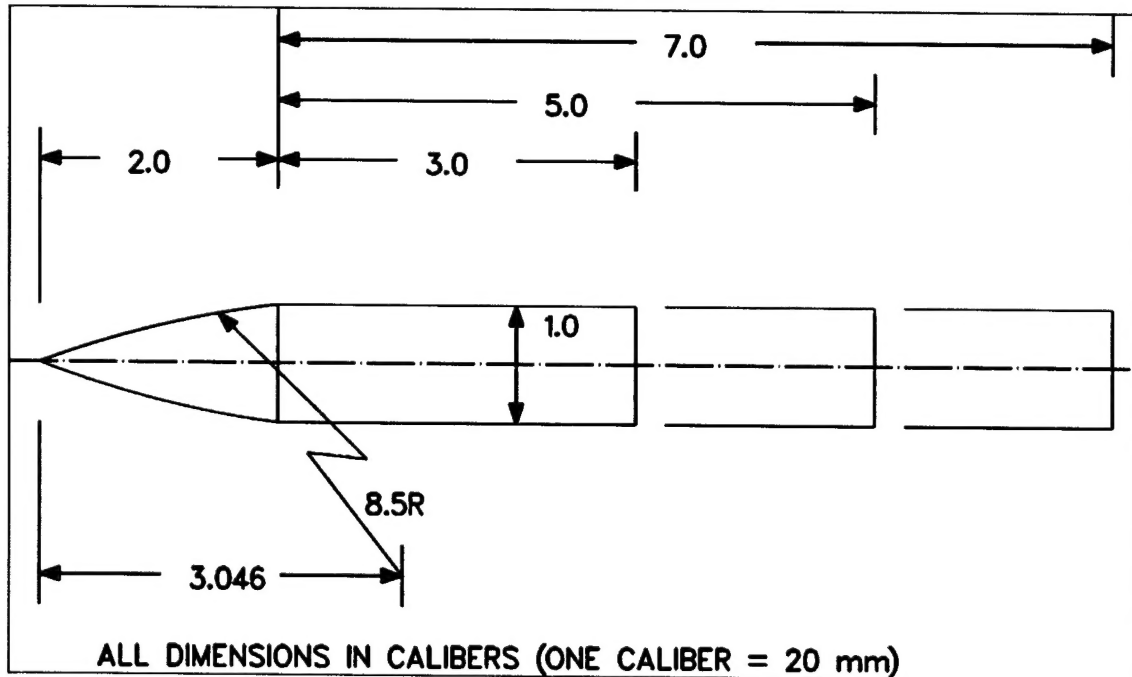


Figure 1. Schematic of ANSR rocket configuration.

1.1 Slender Body Theory Relationships

The slender body theory suggested by Munk (12) and applied by Wood and Murphy (13) among others, allows for simple, though approximate, evaluation of both the static and dynamic aerodynamic coefficients needed to characterize the pitch-damping characteristics of a flight body. The slender body theory allows the forces and moment to be computed from the local body diameter, \hat{D} . For an axisymmetric body, the slender body theory results for the static and dynamic force and moment coefficients can be summarized in the following equations:

Static Coefficients

Normal force coefficient slope:

$$C_{N_\alpha} = \int_0^x \frac{d2\hat{D}^2}{d\bar{x}} d\bar{x} = 2\hat{D}^2. \quad (1)$$

Moment coefficient slope:

$$C_{m_\alpha} = \int_0^x (x_{cg} - \bar{x}) \frac{d2\hat{D}^2}{d\bar{x}} d\bar{x}. \quad (2)$$

Damping Force Coefficients

Force coefficient slope due to angular rate associated with angle of attack:

$$C_{N_{\dot{\alpha}}} = \int_0^x 2\hat{D}^2 d\bar{x}. \quad (3)$$

Force coefficient slope due to transverse angular velocity:

$$C_{N_q} = - \int_0^x \frac{d}{d\bar{x}} [(x_{cg} - \bar{x}) 2\hat{D}^2] d\bar{x} = -2\hat{D}^2 (x_{cg} - x). \quad (4)$$

Damping Moment Coefficients

Moment coefficient slope due to angular rate associated with angle of attack:

$$C_{m_{\dot{\alpha}}} = \int_0^x (x_{cg} - \bar{x}) 2\hat{D}^2 d\bar{x}. \quad (5)$$

Moment coefficient slope due to transverse angular velocity:

$$C_{m_q} = - \int_0^x (x_{cg} - \bar{x}) \frac{d}{d\bar{x}} [(x_{cg} - \bar{x}) 2\hat{D}^2] d\bar{x}. \quad (6)$$

It should be noted that since the upper limit of integration in equations 1–6 is the local axial distance from the nose, the integrated aerodynamic coefficients represent the accumulated force or moment from the nose to local axial position on the body. By substituting the total body length as the upper limit of integration allows the aerodynamic coefficients to be evaluated for the complete body. Thus, these integrals allow both the global aerodynamic coefficients and their distribution along the body to be determined.

The pitch-damping moment coefficient sum $C_{m_q} + C_{m_{\dot{\alpha}}}$ is of considerable practical importance in assessing stability and is easily determined from the sum of equations 5 and 6.

$$C_{m_q} + C_{m_{\dot{\alpha}}} = -2\hat{D}^2 (x_{cg} - x)^2. \quad (7)$$

The slender body theory allows all of the aerodynamic coefficients of interest to be related to the local cross-sectional area of the body as previously seen. Because the aerodynamic coefficients are related to a local property of the body, the theory cannot account for such known effects as "carry-over lift," which is produced in a transition region downstream of the junction between the nose and the cylinder. As a consequence, the normal force coefficient predicted by the slender body theory is known to be incorrect except where the body diameter is rapidly changing. Exactly the same slender body formulas can be obtained from a more sophisticated analysis such as that of Bryson (14). These relations can also be found in the standard reference by Nielsen (15). Bryson's analysis is a general application of the apparent additional mass concept to bodies of more general cross-sectional geometries.

Figure 2 shows comparisons of the slender body and PNS predictions of the normal force coefficient slope for the ANSR. This figure reveals several important and well-known characteristics of slender body theory. First, on the nose of the body where the body diameter is changing, slender body theory predicts the normal force fairly well. However, slender body theory fails to predict the carry-over lift on the cylinder behind the nose. The carry-over lift is significant as it accounts for more than 30% of the normal force. The normal force coefficient also exhibits a Mach number dependence not found in the slender body theory. Since the normal force is independent of the center of gravity location, the same data applies to shorter bodies truncated at any appropriate length.

Similar comparisons are obtained when the slender body theory results for the pitch-damping force coefficients are compared with PNS predictions as shown in Figure 3. Again, the pitch-damping force coefficients are relatively well predicted on the nose, but a significant difference is again seen on the cylinder behind the nose. For both the normal force and pitch-damping force coefficients, slender body theory only provides a qualitative prediction of the force distributions though the error is likely greater than that desired for many preliminary design applications.

1.2 Relationships Between Coefficients

One of the implications of the application of slender body theory is that many of the aerodynamic coefficients appear to be related to one another. In particular, equation 1 provides a direct algebraic relationship between C_{N_α} and \hat{D} . Because of this relationship, all of the coefficients previously shown can be related to C_{N_α} in some manner.

If this view is applied to the pitching moment coefficient, the following is obtained:

$$C_{m_\alpha} = \int_0^x (x_{cg} - \bar{x}) \frac{dC_{N_\alpha}}{d\bar{x}} d\bar{x}. \quad (8)$$

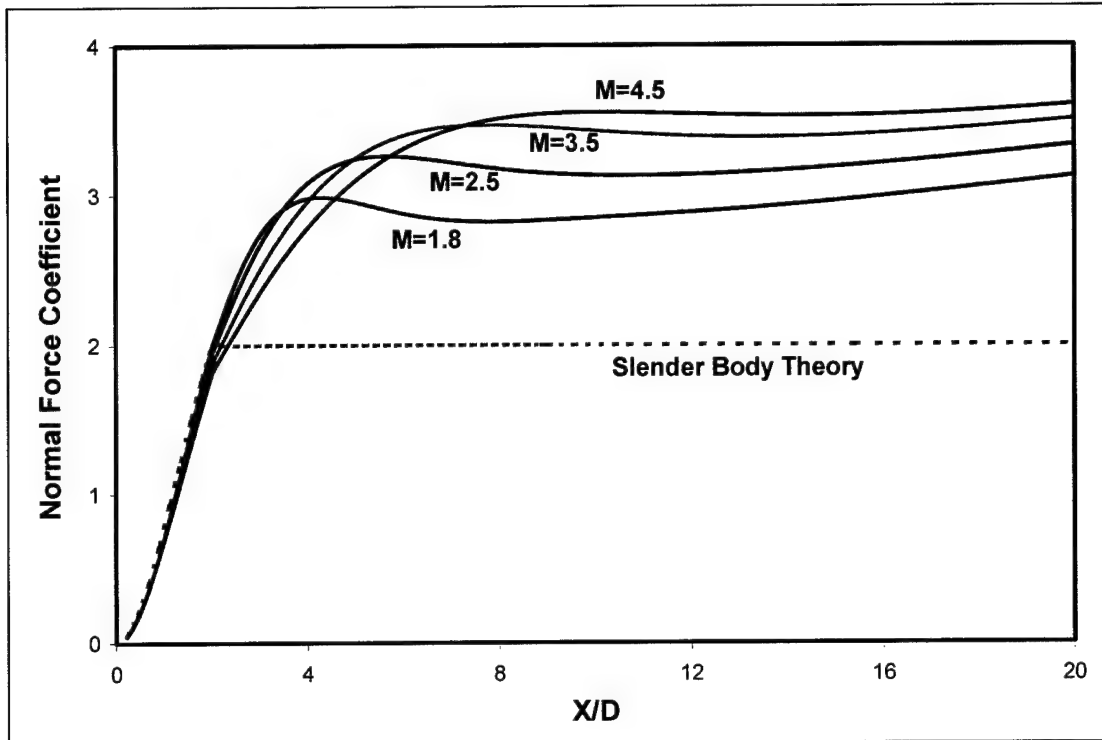


Figure 2. Comparison of predicted normal force coefficient slope $C_{N\alpha}$ distribution with slender body theory for the ANSR.

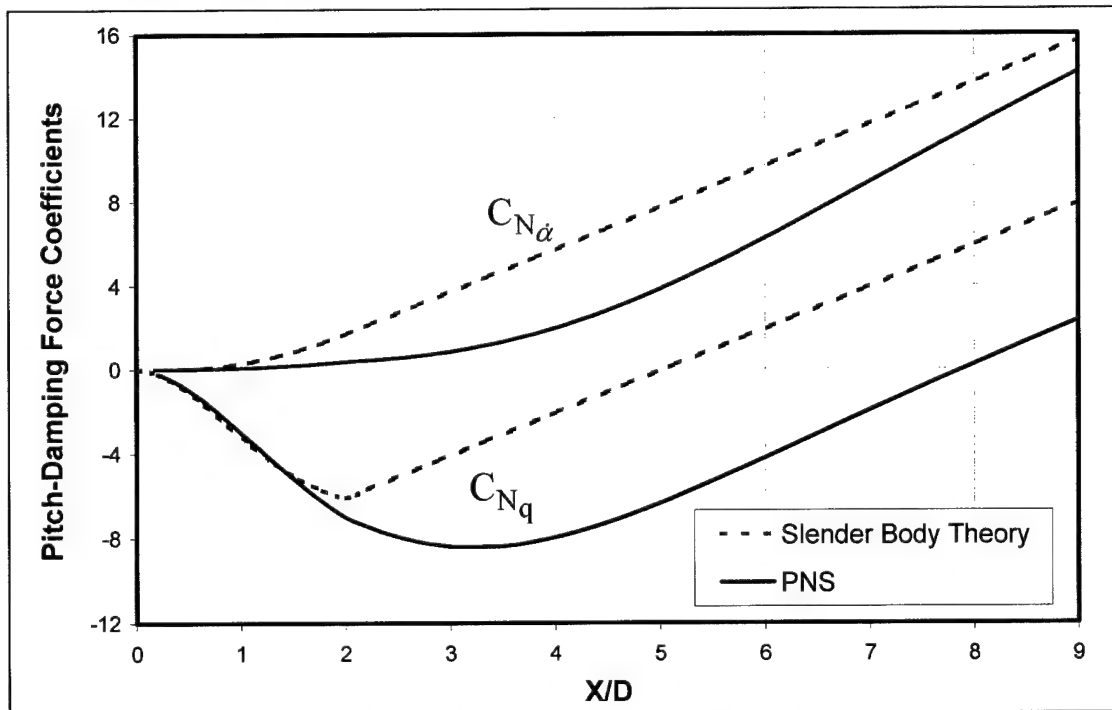


Figure 3. Comparison of PNS and slender body theory predictions of pitch-damping force coefficients over body, ANSR, Mach 2.5, $X_{cg}/D = 5.038$.

This relationship is just the definition of the moment in terms of the distribution of forces written in coefficient form. This suggests that the slender body equations can be used to derive relationships between variables even though the slender body equations in terms of the body geometry are inaccurate. (It should be noted that this form of the pitching moment includes only the contribution from the normal force and ignores the small contribution from the asymmetrical longitudinal forces acting on the nose. This contribution can be shown to produce a small restoring moment. In the results presented here, the computed values of $C_{m\alpha}$ from the more elaborate CFD computation that includes this additional contribution have been used, rather than the value of $C_{m\alpha}$ from equation 8.)

Similarly, the pitch-damping force coefficient $C_{N\dot{\alpha}}$ becomes

$$C_{N\dot{\alpha}} = \int_0^x C_{N\alpha} d\bar{x}. \quad (9)$$

In this form, the pitch-damping force coefficient $C_{N\dot{\alpha}}$ is related to the area under the normal force coefficient curve rather than twice the volume of the body according to slender body theory. This will be shown to be inaccurate, but forms a starting point for an approximation. The pitch-damping force coefficient C_{Nq} can be obtained by differentiating the integrand of equation 4 by parts, i.e.,

$$C_{Nq} = \int_0^x 2\hat{D}^2 d\bar{x} - \int_0^x (x_{cg} - \bar{x}) \frac{d 2\hat{D}^2}{d\bar{x}} d\bar{x}. \quad (10)$$

Both terms of equation 10 can be replaced by the corresponding slender body coefficients,

$$C_{Nq} = C_{N\dot{\alpha}} - C_{m\alpha}. \quad (11)$$

Equation 11 was derived by Sacks (16) using the Blasius method of calculating the forces and moments on a slender body from the cross-flow potential. This result might have been more useful if he had not used the integrated form of the equation for C_{Nq} (equation 4) which gives rather poor results. Equation 11 is also somewhat remarkable because it shows that the two dynamic derivatives C_{Nq} and $C_{N\dot{\alpha}}$ are related to each other and the difference between the two coefficients is the pitching moment slope $C_{m\alpha}$ which is a static aerodynamic coefficient. It is also important to note that the derivation of equation 11 presented here applies only to axisymmetric bodies, though it is possible to show that this relationship holds for bodies with more general cross sections (14, 16).

The pitch-damping moment coefficient becomes

$$C_{m\dot{\alpha}} = \int_0^x (x_{cg} - \bar{x}) \frac{dC_{N\dot{\alpha}}}{d\bar{x}} d\bar{x} = \int_0^x (x_{cg} - \bar{x}) C_{N\alpha} d\bar{x}. \quad (12)$$

This form is in direct analogy with the pitching moment and normal force relationship.

The integrand of the damping moment due to transverse angular rate in equation 6 can also be expanded into two parts, which can be identified as follows:

$$C_{m\dot{\alpha}} = C_{m\dot{\alpha}} - C_{2m\alpha}. \quad (13)$$

The static pitching second moment slope $C_{2m\alpha}$ represents an additional term defined as

$$C_{2m\alpha} = \int_0^x (x_{cg} - \bar{x})^2 \frac{dC_{N\alpha}}{d\bar{x}} d\bar{x}. \quad (14)$$

The relationship shown in equation 13 is analogous to the form for the force coefficients shown in equation 11. The damping moment $C_{m\dot{\alpha}}$ can also be expressed as a function of C_{Nq} in a manner analogous to the damping moment $C_{m\dot{\alpha}}$:

$$C_{m\dot{\alpha}} = \int_0^x (x_{cg} - \bar{x}) \frac{dC_{Nq}}{d\bar{x}} d\bar{x}. \quad (15)$$

Finally, the sum of the pitch-damping moment coefficients becomes

$$C_{m\dot{\alpha}} + C_{m\dot{\alpha}} = -C_{N\alpha} (x_{cg} - x)^2. \quad (16)$$

Note that all the coefficient relationships (equations 8, 9, and 11–13) are consistent with the translation of the center of gravity relations, as are the slender body theory equations.

In this form, all the aerodynamic coefficients of interest are related in some manner to the normal force distribution rather than the local cross-sectional area of the body. Part of the motivation for casting the aerodynamic coefficients in this form is that it may be possible to overcome some of the shortcomings of slender body theory, such as the lack of history effects, because some of the history effects are already contained in the normal force distribution. Second, the normal force distribution is readily obtainable from current fast design approaches such as AP98 (7) and DATCOM (8). Thus, a method for predicting the pitch-damping coefficients based on the normal force distribution can be easily used in conjunction with existing fast design methods eliminating the need to correlate the normal force distribution itself.

Figure 4 shows a comparison of the pitch-damping force coefficient $C_{N\dot{\alpha}}$ computed using equation 9 with the CFD predictions of $C_{N\dot{\alpha}}$. In applying equation 9, the predicted normal force distribution from CFD was used. The application of equation 9 appears to overestimate $C_{N\dot{\alpha}}$ by about 60% compared with the CFD predictions. However, the distribution of the force along the body is similar for both results.

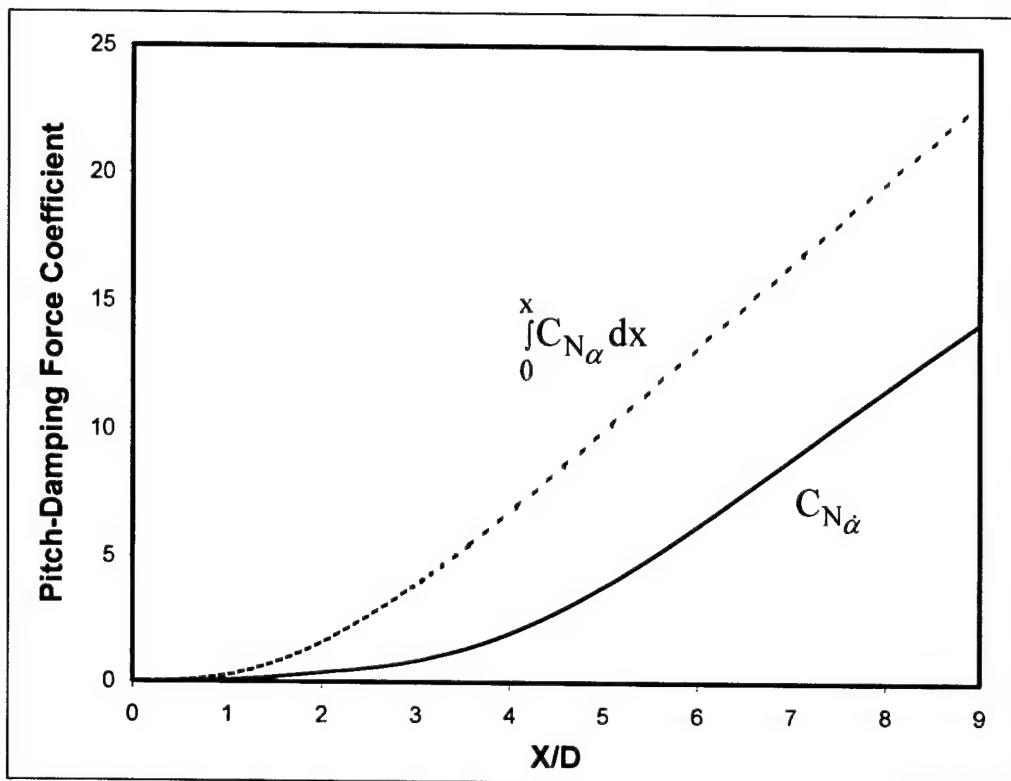


Figure 4. Comparison of pitch-damping force coefficient $C_{N\dot{\alpha}}$ with integral of normal force coefficient over body, Mach 2.5, ANSR, CFD predictions.

Figure 5 shows a comparison of the pitch-damping force coefficient C_{N_q} computed using Sacks's relation (equation 11) with the CFD predictions of C_{N_q} . The pitch-damping coefficient distribution required in equation 11 was obtained from CFD. Over the nose region, equation 11 yields an accurate prediction of C_{N_q} , though the accuracy is degraded somewhat over the rear of the body. Equation 11 does provide enhanced accuracy compared with the direction application of slender body theory shown in Figure 3. (Weinacht and Danberg [17] provide a more complete discussion of the relative accuracy of Sacks's relation.)

The results shown in Figures 4 and 5 demonstrate that casting the original slender body theory results in terms of the normal force coefficient does allow some improvement in the predictive capability. However, further effort is required to establish a predictive capability using these relations with sufficient accuracy for design applications.

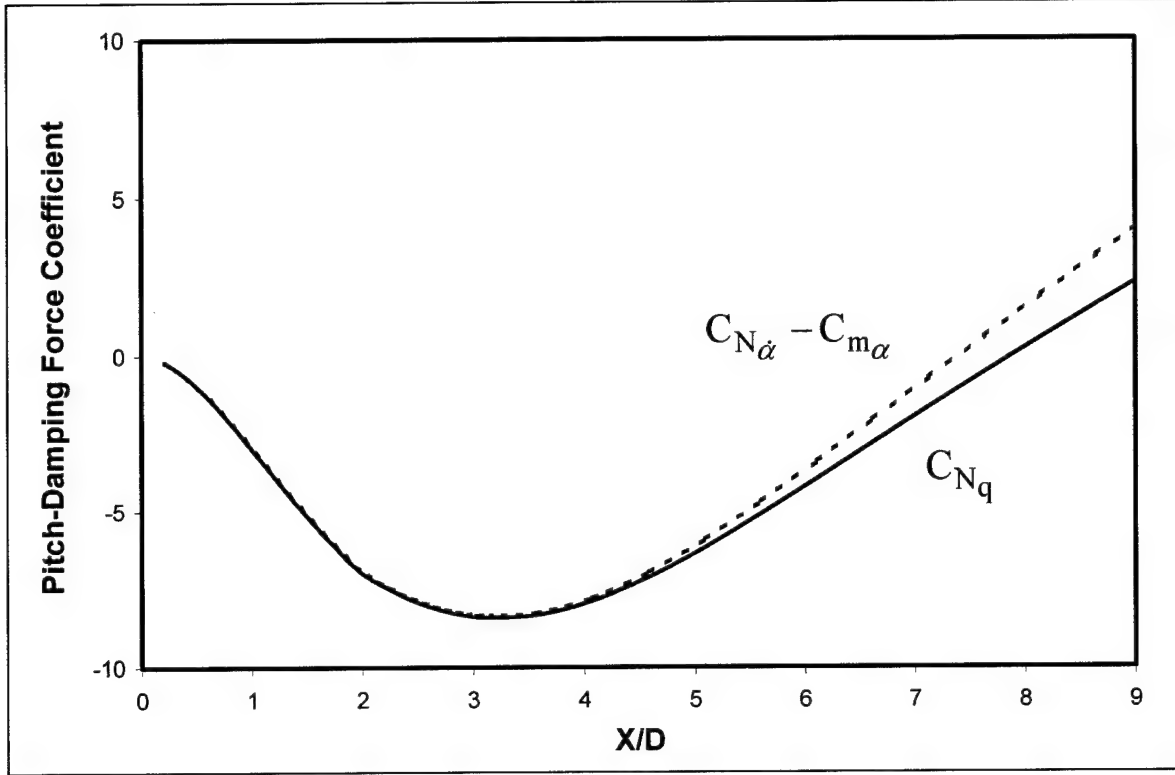


Figure 5. Comparison between C_{Nq} and $C_{N\dot{\alpha}} - C_{m\alpha}$ (equation 11), Mach 2.5, ANSR, $X_{cg}/D = 5.038$, CFD predictions.

2. Formulation of an Approximate Model

The critical element in the evaluation of the pitch-damping coefficients is the approximation of $C_{N\dot{\alpha}}$. As can be seen from equations 11, 12, and 15, once $C_{N\dot{\alpha}}$ is determined, the damping coefficients C_{Nq} , $C_{m\dot{\alpha}}$, and C_{mq} can be determined using these equations. The relationship given by equation 9 overestimates $C_{N\dot{\alpha}}$ by about 60% at 9 calibers as is shown in Figure 4.

Both curves, however, are similar in general form. A function, $G(x)$, is introduced into equation 9 multiplying $C_{N\alpha}$ to correct for this discrepancy.

$$C_{N\dot{\alpha}} = \int_0^x G(\bar{x}) C_{N\alpha} d\bar{x}, \quad (17)$$

or alternatively, the function $G(x)$ is defined:

$$G(x) = \frac{1}{C_{N\alpha}} \frac{dC_{N\dot{\alpha}}}{dx}. \quad (18)$$

By applying equation 12, the pitch-damping moment coefficient $C_{m\dot{\alpha}}$ can be expressed in terms of the function $G(x)$.

$$C_{m\dot{\alpha}} = \int_0^x (x_{cg} - \bar{x}) \frac{dC_{N\dot{\alpha}}}{d\bar{x}} d\bar{x} = \int_0^x (x_{cg} - \bar{x}) G(\bar{x}) C_{N\dot{\alpha}} d\bar{x}. \quad (19)$$

The function $G(x)$ can be evaluated from CFD derived values of $C_{N\alpha}$ and $C_{N\dot{\alpha}}$ using equation 18.

Figure 6 shows $G(x)$ for the ANSR in the Mach number range from 1.8 to 4.5. Two distinct regions are seen in Figure 6 corresponding to the ogival nose ($0 < x < 2$) and cylindrical afterbody ($x > 2$).

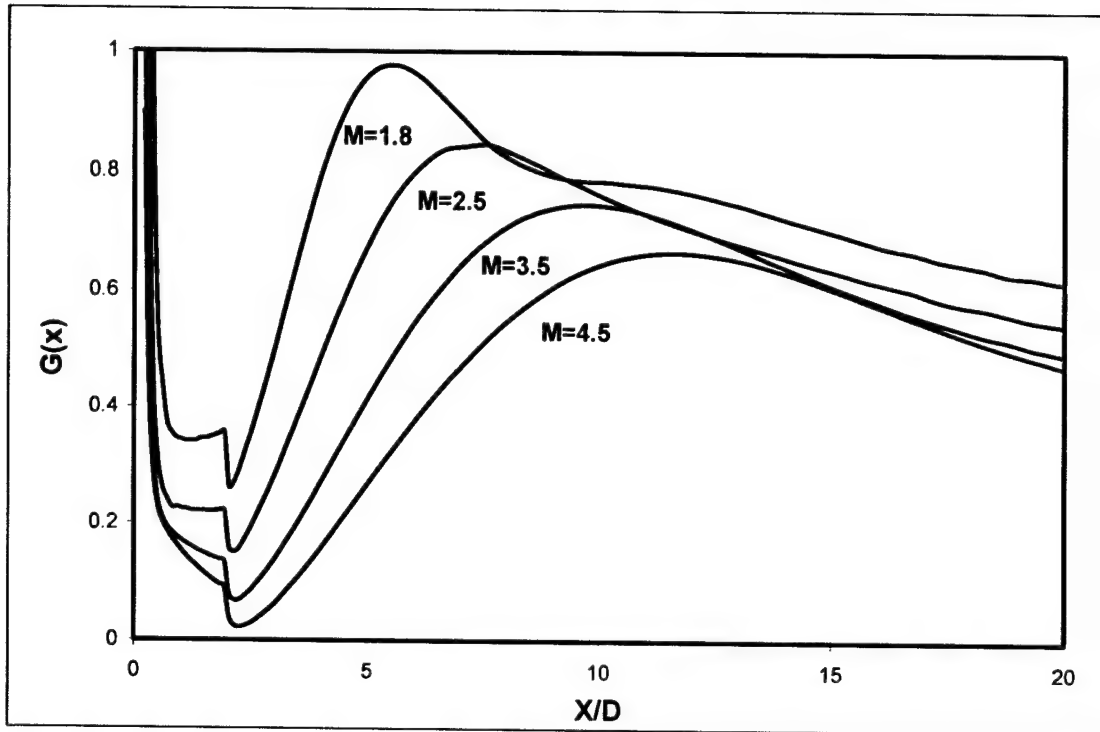


Figure 6. $G(x)$ over the ANSR for various Mach numbers.

On the nose, $G(x)$ is relatively small except near the nose tip. The large values of $G(x)$ very close to the nose tip are believed to be caused by numerical start-up transients associated with the conical starting procedure used in the PNS approach. These transients have little effect on the computed coefficients because both $C_{N\alpha}$ and $C_{N\dot{\alpha}}$ go to zero very rapidly on the nose as the tip is approached. Because $C_{N\dot{\alpha}}$ is so small on the nose, the characterization of $G(x)$ for the nose region is somewhat less important than for the cylindrical afterbody.

2.1 $G(x)$ on Cylinder (Carry-Over Transformation)

Compared to the nose region, the more significant variation in $G(x)$ occurs in the carry-over region after the nose as is shown in Figure 6. Rather than attempt to develop an analytic function to describe $G(x)$ in terms of Mach number and x , the possibility of defining a coordinate

transformation to relate at least a part of $G(x,M)$ to a single function, e.g., $G_{25} = G(X_{25}, M = 2.5)$, is considered.

Figure 6 suggests that, for $x > 2$ but before $G(x)$ reaches a maximum, $G(x)$ is nearly linear with x . In this region, $G(x)$ can be approximated as a linear function for each Mach number, as shown in Figure 7. Furthermore, each curve appears to intersect at a common point, $G(0) = G(x = 0)$. This suggests $G(x)$ can be represented in the form shown in equation 20:

$$G(x, M) = T(M)[G(X_{25}) - G(0)] + G(0), \quad (20)$$

where, in the linear region,

$$X_{25} = \frac{S(M)}{T(M)} x; \quad (21)$$

$$S(M) = \frac{\left(\frac{dG}{dx}\right)_{\text{linear}}}{\left(\frac{dG_{25}}{dX_{25}}\right)_{\text{linear}}}. \quad (22)$$

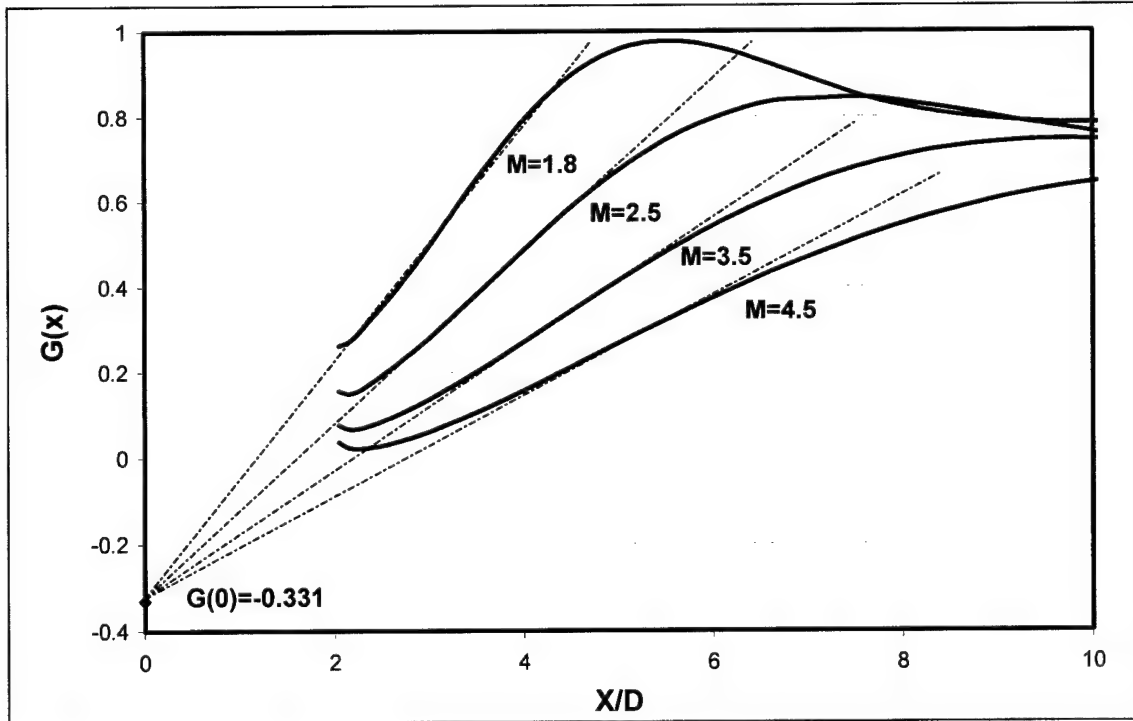


Figure 7. Correlation of $G(x)$ on the cylindrical afterbody, ANSR.

On the cylindrical body, G_{25} is obtained from a table look-up and interpolation based on the transformation of x given by equation 21. An abbreviation of the reference data is given in Table 1. Local values of G are obtained from equation 20 where $G(0) = -0.331$.

Table 1. G_{25} as a function of X_{25} .

X_{25}	$G_{25}(X_{25})$
0.	-0.331
1.	-0.127
2.	0.076
3.	0.281
4.	0.486
5.	0.674
6.	0.796
7.	0.842
8.	0.835
9.	0.799
10.	0.763
11.	0.730
12.	0.703
13.	0.680
14.	0.658
15.	0.636
16.	0.615
17.	0.595
18.	0.576
19.	0.558
20.	0.543

The similarity factor T accounts for the decrease in the maximum $G(x)$ with Mach number. The x coordinate transformation factor S is equal to the ratio of the slopes of the linear regions. Based on the PNS data for the ANSR, the curve fits were obtained for the $S(M)$ and $T(M)$ and are shown in equations 23 and 24. The variation of the factors $S(M)$ and $T(M)$ with Mach number is also shown in Figure 8.

$$S(M) = 0.0688 + 2.302 \frac{1}{M} + 0.0718 \frac{1}{M^2}. \quad (23)$$

$$T(M) = 0.615 + 1.176 \frac{1}{M} - 0.510 \frac{1}{M^2}. \quad (24)$$

Figure 9 shows the resulting transformation of the $G(x)$ distributions of Figure 6. The data in the carry-over region are very well represented by a single curve, although there is some divergence in the different Mach number curves beyond the peak in the data. Thus, some error in the final results for large L/D_{ref} bodies must be accepted.

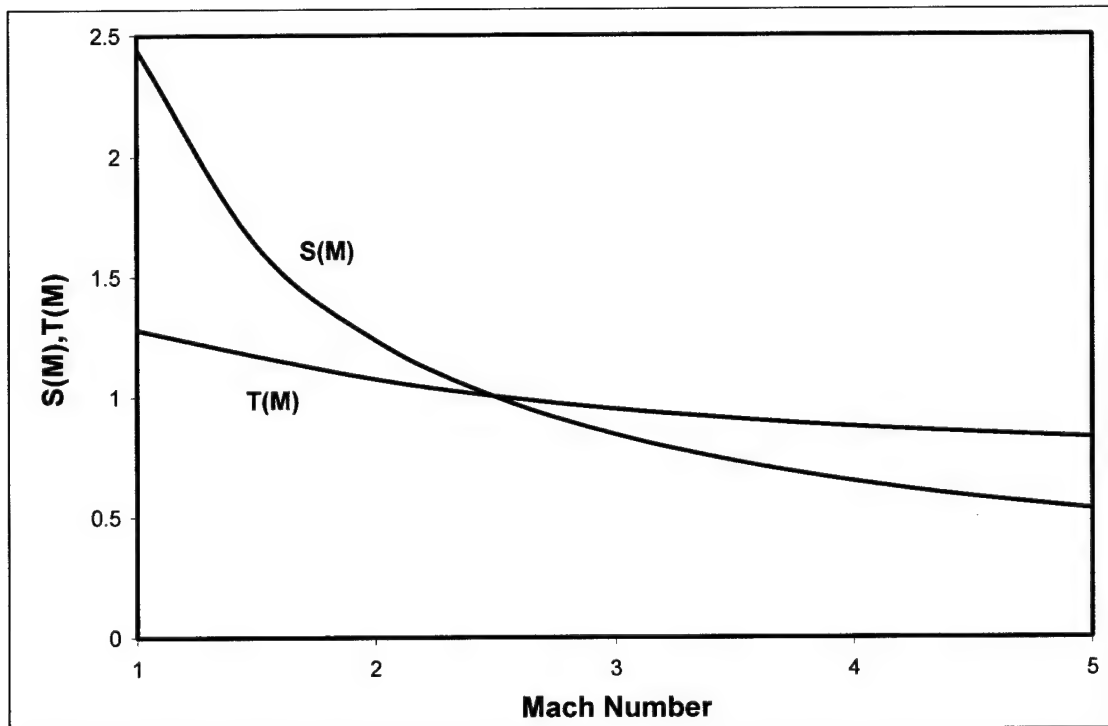


Figure 8. Similarity factors $S(M)$ and $T(M)$.

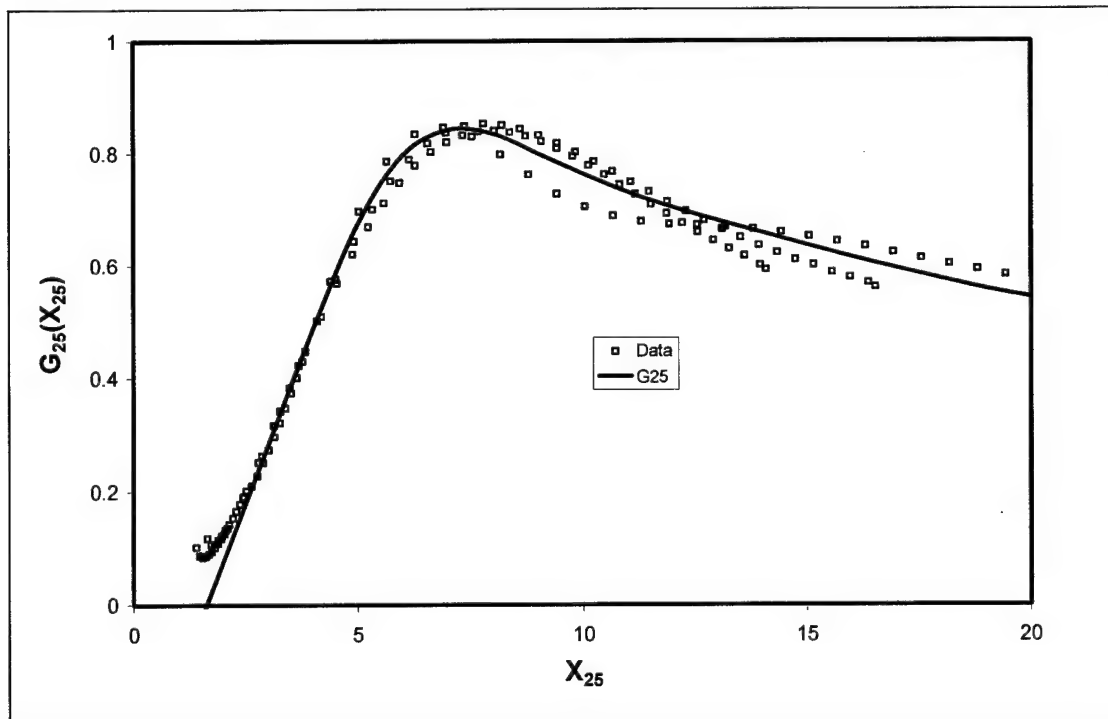


Figure 9. Correlation of $G_{25}(X_{25})$ with computed data, ANSR.

2.2 Effect of Nose Length

The previous analysis has considered only a fixed nose length of 2 calibers. When nose length is varied, changes in the distribution of $G(x)$ become apparent. Figure 10 shows the distribution of $G(x)$ for a tangent-ogive/cylinder configuration with nose lengths of 2, 4, 6, and 8 calibers at Mach 2.5. While the shape of the curves behind the nose/cylinder junction remain relatively the same, the curve shift upwards and to the right with increasing nose length. The shift of the curve to the right with increasing nose length might be expected because of the shift in the location of the nose/cylinder junction. The upward shift in $G(x)$ is perhaps less intuitive. To account for the shift in the curve with increasing nose length, the following correction was added to the original correlation previously shown.

$$G(x, M) = T(M) \left[G_{25}(X_{25}) - G(0) + 0.0183 \left(\frac{L_{\text{nose}}}{D} - 2 \right) \right] + G(0); \quad (25)$$

$$X_{25} = \frac{S(M)}{T(M)} \left[x - 0.5833 \left(\frac{L_{\text{nose}}}{D} - 2 \right) \right]. \quad (26)$$

When the L/D ratio of the nose L_{nose}/D approaches 2, the correlation reverts to the original form.

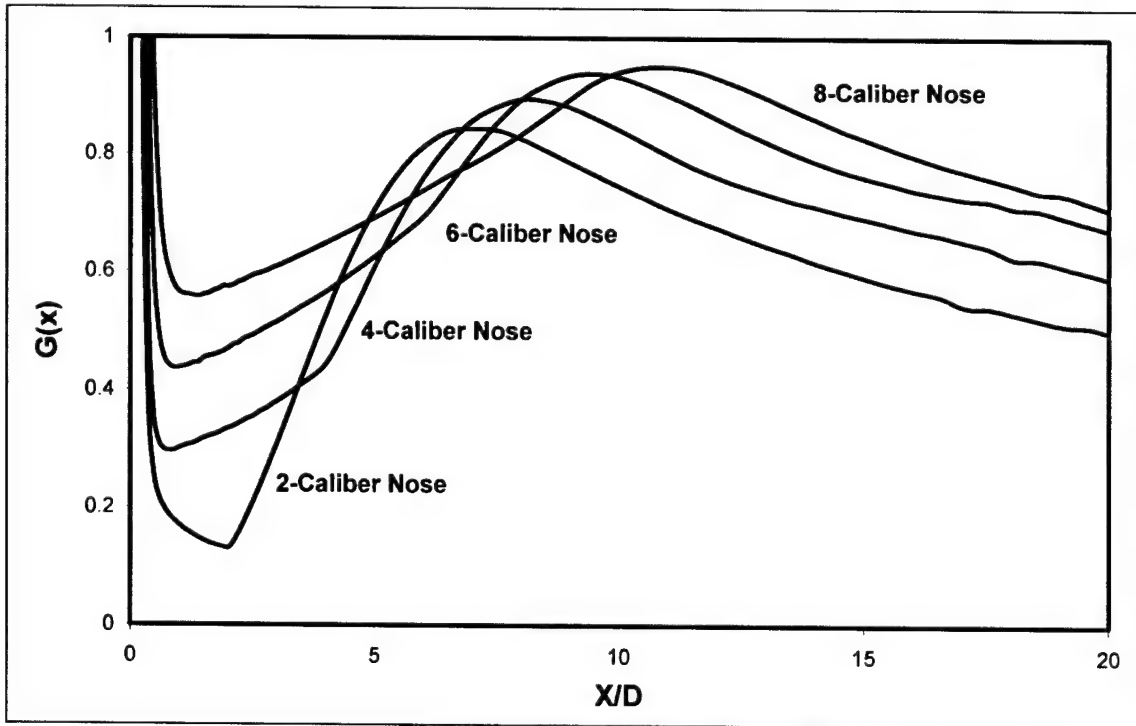


Figure 10. Effect of nose length on $G(x)$, tangent-ogive/cylinder, Mach 2.5.

2.3 Correlation for the Nose Region

In the previous discussion, it was pointed out that the nose region has a relatively small effect on the overall prediction of $C_{N\dot{\alpha}}$. However, to complete the correlation, a suitable evaluation of $G(x)$ for the nose region must be performed. In the course of developing and testing the correlation, it was found that the slope of the nose had a significant effect on the $G(x)$ on the nose, but a much less apparent effect on the carry-over region on the cylinder. To investigate this further, a parametric series of CFD computations for various conical bodies with cone angles from 2° to 28° was performed. In each case, the cone length was sufficient to establish many calibers of constant or near constant $G(x)$ following the tip region transient. Figure 11 shows the results as a function of both the cone angle, θ_C , and Mach number. The initial trend of $G(\text{nose})$ decreasing with Mach number at small values of cone angle is reversed at larger cone angles beginning after 8° . Using a curve-fitting procedure, a closed-form expression for $G(\text{nose})$ for the conical noses has been obtained. This allows a straight-forward evaluation of $G(\text{nose})$ for the conical noses in terms of the Mach number and the cone half-angle θ_C in degrees. The values of the coefficients m_i and b_i are listed in Table 2.

$$G(\text{nose}) = M \sum_{i=0}^{i=5} m_i \theta^i + \sum_{i=0}^{i=5} b_i \theta^i. \quad (27)$$

For conical bodies, the correlation function $G(\text{nose})$ yields a very accurate evaluation of $C_{N\dot{\alpha}}$.

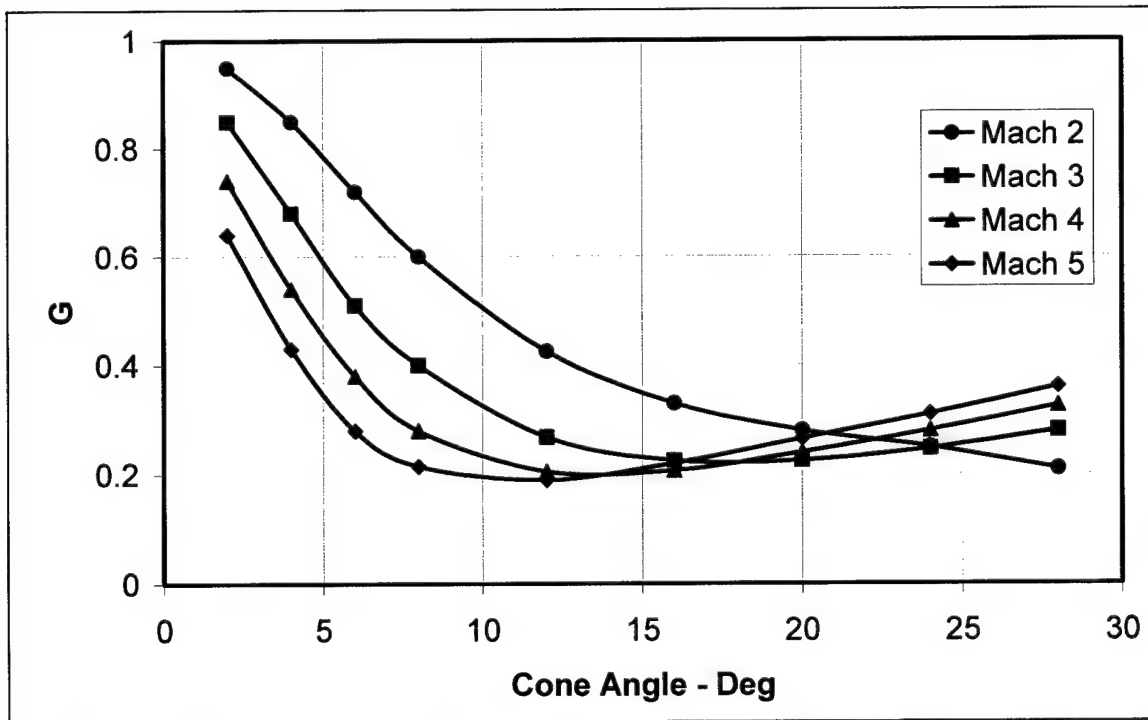


Figure 11. Variation of $G(\text{nose})$ with Mach number and cone angle for conical noses.

Table 2. Coefficients of the fifth-order polynomial fit of equation 27.

i	b_i	m_i
0	1.06724	-0.0137712
1	9.73099×10^{-2}	-6.22894×10^{-2}
2	-2.92027×10^{-2}	9.7226×10^{-3}
3	2.13167×10^{-3}	-5.82041×10^{-4}
4	-6.54121×10^{-5}	1.59364×10^{-5}
5	7.34183×10^{-7}	-1.64649×10^{-7}

This is due, in part, to the fact that $G(x)$ for the conical nose is independent of the location along the nose and is a simple function of Mach number and cone angle. For other nose types, such as ogival noses, $G(x)$ appears to vary along the nose (Figures 6 and 10). However, it was found that a suitable approximation for $G(x)$ on an ogive nose could be obtained by using the $G(\text{nose})$ for a conical nose whose nose tip angle was equal to the slope at the tip of the ogive. For a tangent ogive nose, it can be shown that the local slope at the tip of the nose is equal to twice the cone angle for a conical nose of equivalent length. Thus, typically slopes for ogive noses are about 20° and $G(\text{nose})$ is relatively small.

2.4 Pitch Damping Force, C_{N_q} (Sacks's Relationship)

The pitch damping force due to the transverse angular rate C_{N_q} can be evaluated in terms of $C_{N_{\dot{\alpha}}}$ and the static moment coefficient, $C_{m_{\alpha}}$, from the relation derived by Sacks (i.e., equation 11). The PNS data provides the first accurate test of equation 11 using higher level models. The following residual, H , is computed for the $L/D = 20$ ANSR case:

$$H(x) = C_{N_{\dot{\alpha}}} - C_{m_{\alpha}} - C_{N_q}, \quad (28)$$

and this is shown in Figure 12. For the first 4–5 calibers, the residual is negligible, but for long bodies, the error in equation 11 becomes more important. The difference, H , can be approximated easily as straight lines of slope, $\frac{dH}{dx} = 0.35$. The intercept on the axis, x_H , of these lines is found to be proportional to the same x transformation factor as in the function $G(x)$, i.e., $x_H = 4.35S(M)/T(M)$, where 4.35 is the intercept for the Mach number 2.5 case. The effect of nose length was investigated for $H(x)$. Although some effect of nose length was apparent, the effect was less than the variability in the approximation previously described. Thus, no correction for nose length was applied.

The pitch-damping force and moment coefficients C_{N_q} and C_{m_q} can be computed by appropriately adding the correction $H(x)$ to equations 11 and 13.

$$C_{N_q} = C_{N_{\dot{\alpha}}} - C_{m_{\alpha}} - H(x). \quad (29)$$

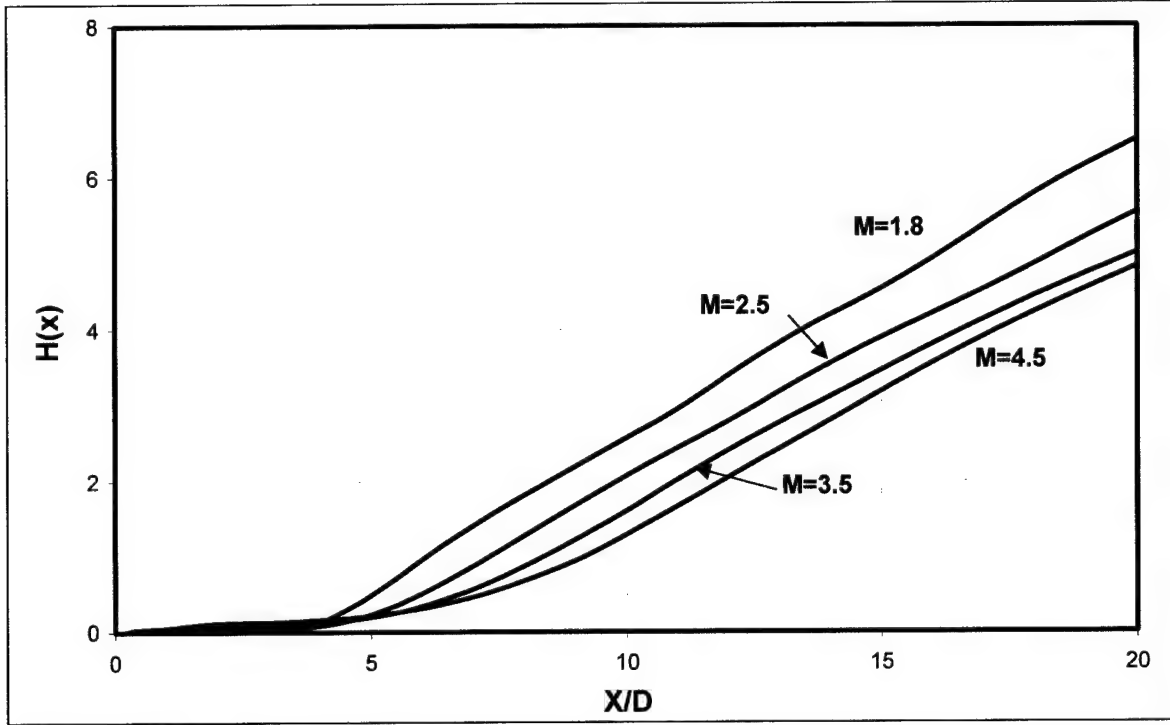


Figure 12. Distribution of $H(x)$ along body for ANSR.

$$C_{m_q} = C_{m_{\dot{\alpha}}} - C_{2m_{\alpha}} - \int_{x_H}^x (x_{cg} - \bar{x}) \frac{dH}{d\bar{x}} d\bar{x}. \quad (30)$$

It should be noted that the correction term $H(x)$ is added to improve the correlation, although it is relatively small. Direct application of equations 11 and 13 provides reasonable estimates of the coefficients C_{N_q} and C_{m_q} . (Weinacht and Danberg [17] further discuss direct application of these relations.)

Figures 13 and 14 show the results of applying the approximate method to the $L/D = 9$ ANSR configuration at Mach 2.5. The comparisons with the PNS results are very good with errors less than 3%. The approximate method is effective in substantially reducing the errors that result from applying slender body theory. The results are typical of those that are obtained using the approximate method for other configurations, although somewhat larger errors may be encountered.

2.5 Pitch-Damping Moment Coefficient Sum

The pitch-damping moment coefficient sum can be easily obtained by adding equations 19 and 30. However, the sum of these two equations can be recast into a form, shown in equation 31, that better illustrates the effect of the correlation terms.

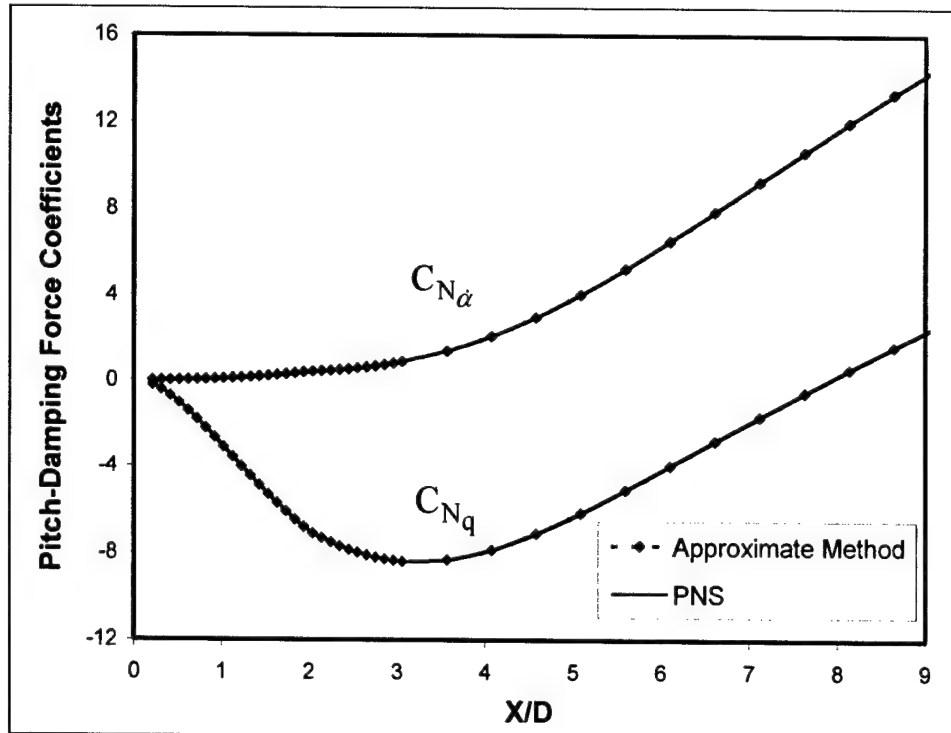


Figure 13. Comparison of PNS and approximate method predictions of pitch-damping force coefficients over body, ANSR, Mach 2.5, $X_{cg}/D = 5.038$.

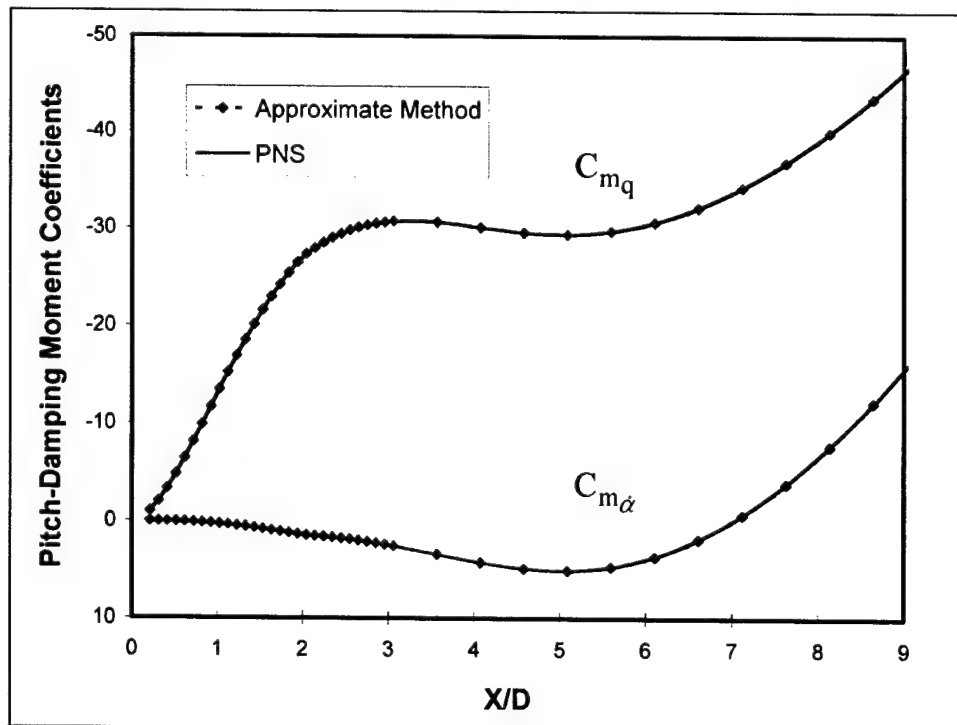


Figure 14. Comparison of PNS and approximate method predictions of pitch-damping moment coefficients over body, ANSR, Mach 2.5, $X_{cg}/D = 5.038$.

$$C_{m_q} + C_{m_{\dot{\alpha}}} = -(x_{cg} - x)^2 C_{N_{\alpha}} - \int_0^x 2(1 - G)(x_{cg} - \bar{x}) C_{N_{\alpha}} d\bar{x} - \int_{x_H}^x (x_{cg} - \bar{x}) \frac{dH}{d\bar{x}} d\bar{x}. \quad (31)$$

The first term on the right-hand side is the slender body theory result using the normal force coefficient slope (equation 16). Note that in either form of the slender body theory (equations 7 or 16), the pitch-damping moment coefficient goes to zero at the center of gravity. The second term of equation 31 takes into account upstream effects and it is this term that prevents the moment sum from going to zero at the center of gravity. This is illustrated with Figure 15, which presented results for the 9-caliber ANSR. The large difference between the slender body theory and the PNS results are most significant around the center of gravity. Note also that the integrand of the second term of equation 31 changes sign at the center of gravity. By appropriately locating the center of gravity, this integral can be made to cancel out for a given body producing apparently good (though fortuitous) predictions of the pitch-damping coefficient sum using slender body theory for some center of gravity locations. The last integral term accounts for the discrepancy in Sacks's relationships (equations 11 and 13), and its contribution is typically smaller than the second term. Although equation 31 is more complicated than slender body theory, it does account for the effect of the force carry-over from the nose onto the cylindrical afterbody that is necessary to produce an accurate evaluation of the pitch-damping moment coefficient sum.

2.6 Reynolds Number Effects

The effect of the Reynolds number on the correlation parameters was also considered during the course of the study because of its possible effect on the carry-over lift. The ANSR configuration was used as the reference configuration for the study. For the results presented here, all the Navier-Stokes results are computed at standard sea level conditions. As a consequence, the actual Reynolds number, for each geometry, varies linearly with Mach number. In the investigation of Reynolds number effects, the Reynolds number was changed by constant factors ($Re_r = 0.5, 2, 5, 10$) holding the flight velocity and Mach number unchanged. This can be interpreted as a variation in the reference diameter from 10 to 200 mm for the ANSR, which has a nominal diameter of 20 mm. The magnitude of the Reynolds number = $454,000 M Re_r$. The results show some variation near the maximum in the carry-over region of the G curve but the magnitude of the effect on the pitch-damping moment coefficient was only between 2% and 4% and is not considered further.

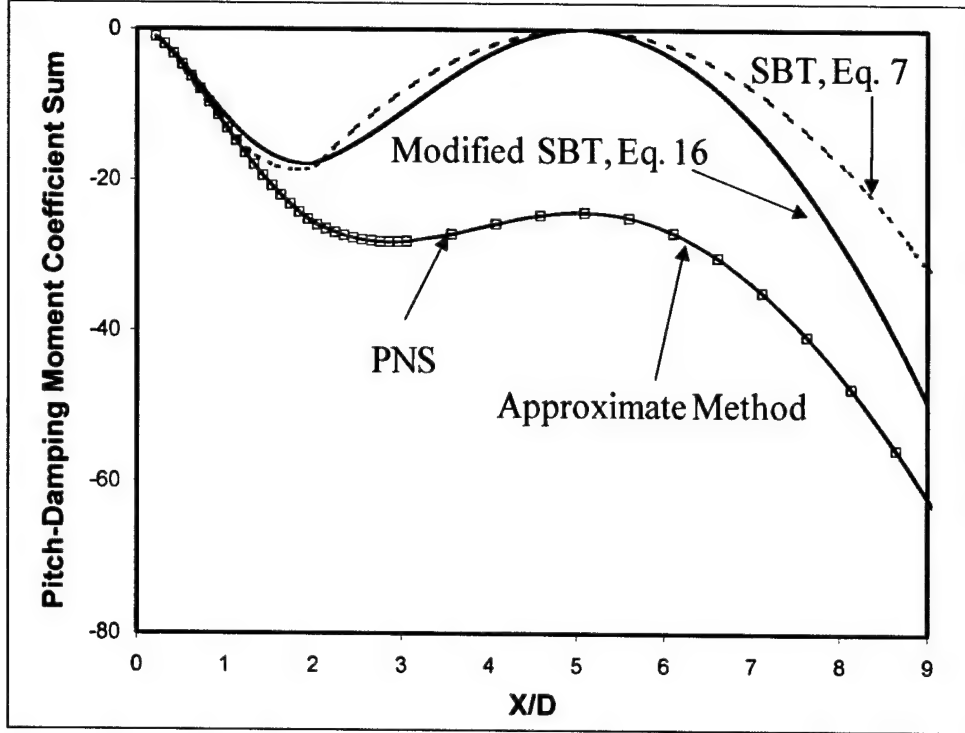


Figure 15. Comparison of slender body theory, PNS, and approximate method predictions of pitch-damping moment coefficient sum over body, ANSR, Mach 2.5, $X_{cg}/D = 5.038$.

3. Application of the Approximate Model

The accuracy of the approximate model was assessed by comparison with both experimental data and computational predictions. An important element in the experimental comparisons is the accuracy of the approximate method relative to the typical experimental error from range experiments. Due to the limited experimental data available, the computational predictions were utilized to perform a more complete evaluation of the model for a variety of geometries and flight conditions not available in the current experimental database. Errors were quantified in terms of the individual error Δ for each one-to-one comparison and the overall root mean square (rms) deviation, σ , for complete datasets containing N individual comparisons.

$$\Delta = \frac{(C_{mq} + C_{m\dot{\alpha}})_{\text{Correlation}} - (C_{mq} + C_{m\dot{\alpha}})_{\text{Data}}}{(C_{mq} + C_{m\dot{\alpha}})_{\text{Data}}} \quad (29)$$

$$\sigma = \sqrt{\frac{1}{N} \sum_{i=1}^N \Delta^2} \quad (30)$$

The experimental database for the ANSR rocket is probably the highest quality experimental database for evaluating the pitch-damping predictions for axisymmetric flight bodies. The database includes three different body lengths; 5-, 7-, and 9-caliber bodies; with three center of gravity locations for each body length at Mach 1.3, 1.8, and 2.5. Figure 16 shows a comparison of the predicted pitch-damping moment coefficient sum using the approximate model with the experimental database. In general, no consistent bias in the predicted data is observed. The rms derivation, σ , is 18% for the complete dataset; however, this error includes the variability in the experimental data. The experimental variability is evident because multiple firings were performed for the same geometry and flight conditions and multivalued data were obtained for the same flight conditions. Figure 17 shows the comparisons between the approximate model with CFD predictions. The approximate model appears to show a small consistent overprediction of the pitch-damping moment coefficient sum for this dataset. Here, the rms derivation, σ , is 11% and is perhaps better representative of the overall accuracy of the model. This overprediction is not evident in the comparisons with experimental data due to the experimental uncertainty.

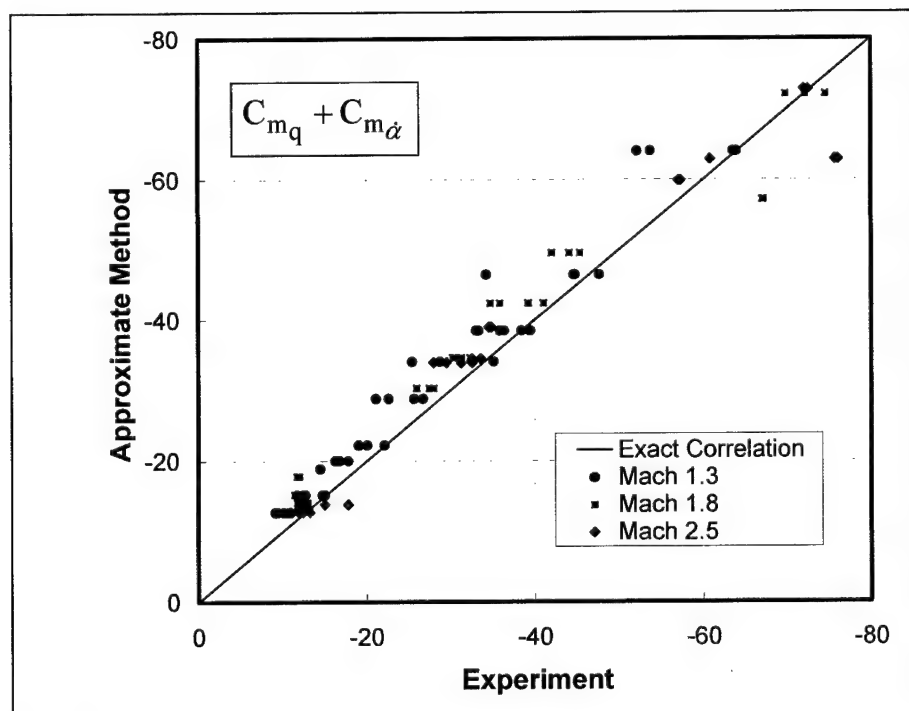


Figure 16. Correlation between approximate method predictions and experimental data for $C_{m_q} + C_{m_{\dot{\alpha}}}$, ANSR, L/D = 5, 7, and 9, and Mach 1.3, 1.8, and 2.5.

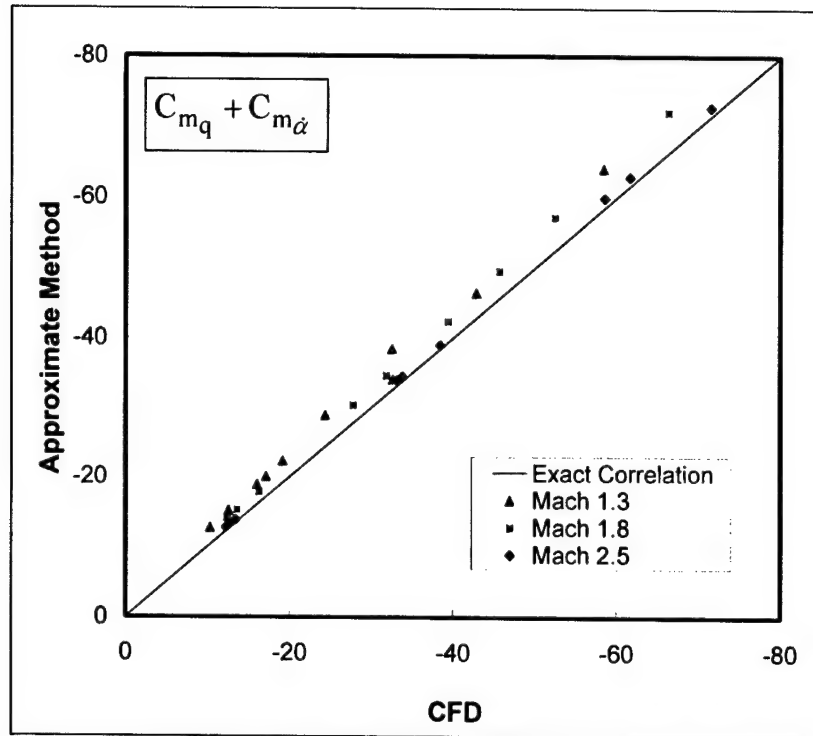


Figure 17. Correlation between approximate method predictions and CFD computations for $C_{m_q} + C_{m_{\dot{\alpha}}}$, ANSR, $L/D = 5, 7$, and 9 , and Mach $1.3, 1.8$, and 2.5 .

The accuracy of the approximate model was also evaluated by comparing the results of the model with CFD predictions of the pitch-damping moment coefficient sum for a series of tangent ogive/cylinder and cone/cylinder body geometries. In this study, a variety of nose lengths were considered: 2, 2.5, 3, 4, 5, 6, and 8 calibers and body lengths from 5 to 20 calibers. All bodies had at least 1 caliber of cylindrical afterbody. Thus, not all nose lengths were considered for bodies less than 9 calibers in length. Mach numbers of 2, 3, 4, and 5 were also considered. For each body length, a fixed center of gravity location for each body length was used as shown in Table 3. Realistically, the center of gravity location should be expected to move rearward for larger nose lengths for monolithic bodies, although fixing the nose length at a specified location does allow the aerodynamic effects to be isolated from the effects produced by center of gravity shift.

Figures 18 and 19 compare the results of the application of the approximate method with the CFD predictions for the tangent ogive cylinder and cone cylinder bodies for the pitch-damping moment sum, $C_{m_q} + C_{m_{\dot{\alpha}}}$. In general, the results of applying the approximate method compare well with the CFD predictions with relatively little bias in the results across the range of parameters tested.

For the tangent ogive cylinder body, the maximum error between the approximate method and the CFD predictions was 25% with an overall rms deviation, σ , of 9%. For the cone cylinder

Table 3. Center of gravity locations
as a function of body length.

L/D	X_{cg}/D
5.	3.0
7.	4.037
9.	5.038
12.	6.565
15.	8.063
20.	10.565

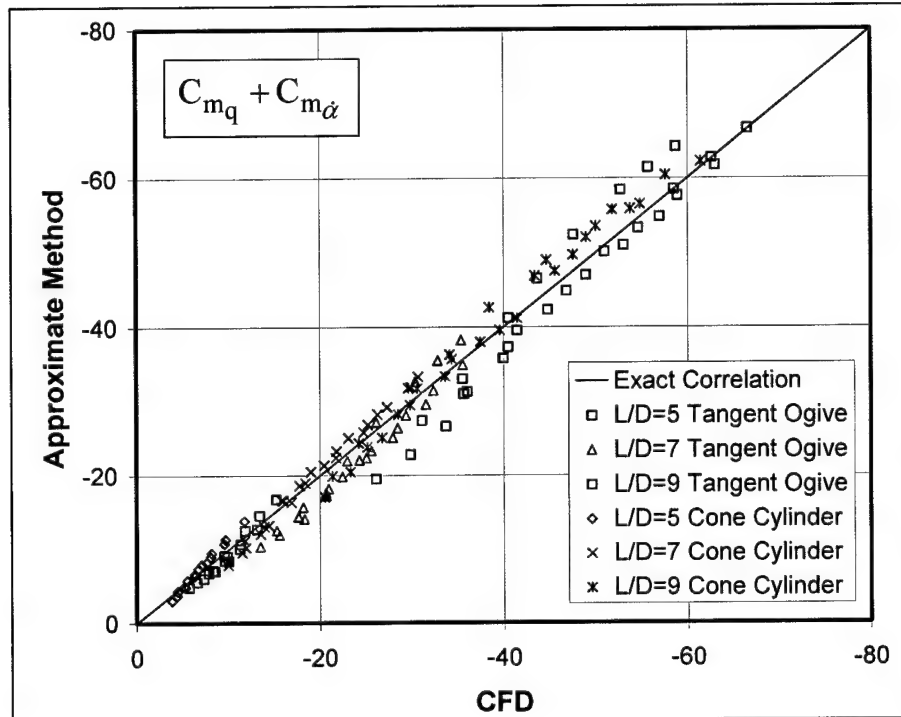


Figure 18. Correlation between approximate method predictions and CFD computations for $C_{m_q} + C_{m_{\dot{\alpha}}}$, cone cylinder and tangent ogive cylinder bodies, $L/D = 5, 7$, and 9 .

body, the maximum error between the approximate method and the CFD predictions was 21% with an overall rms deviation, σ , of 7%. In general, the largest errors were encountered for the smaller L/D bodies.

The comparisons were also made for the individual pitch-damping coefficients $C_{m_{\dot{\alpha}}}$ and C_{m_q} and are shown in Figures 20–23. The comparisons for the pitch-damping coefficient $C_{m_{\dot{\alpha}}}$ show a greater variability than for C_{m_q} . As discussed previously, $C_{N_{\dot{\alpha}}}$ and $C_{m_{\dot{\alpha}}}$ are computed from the normal force distribution and the correlation function $G(x)$ using equations 17 and 19. C_{N_q} and C_{m_q} are then computed from equations 29 and 30 using the computed values of

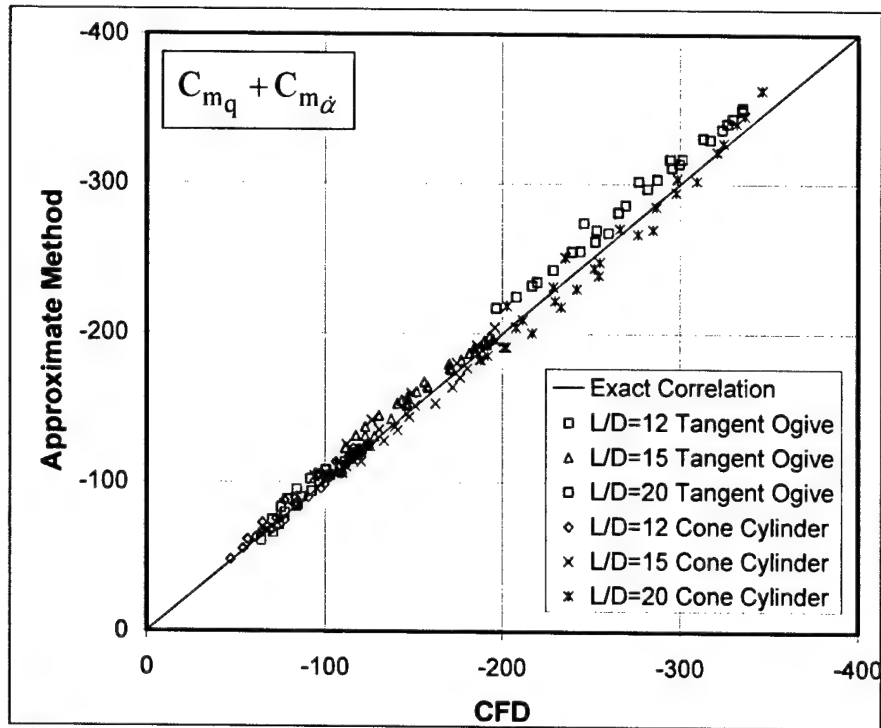


Figure 19. Correlation between approximate method predictions and CFD computations for $C_{m_q} + C_{m_{\dot{\alpha}}}$, cone cylinder and tangent ogive cylinder bodies, $L/D = 12, 15$, and 20 .

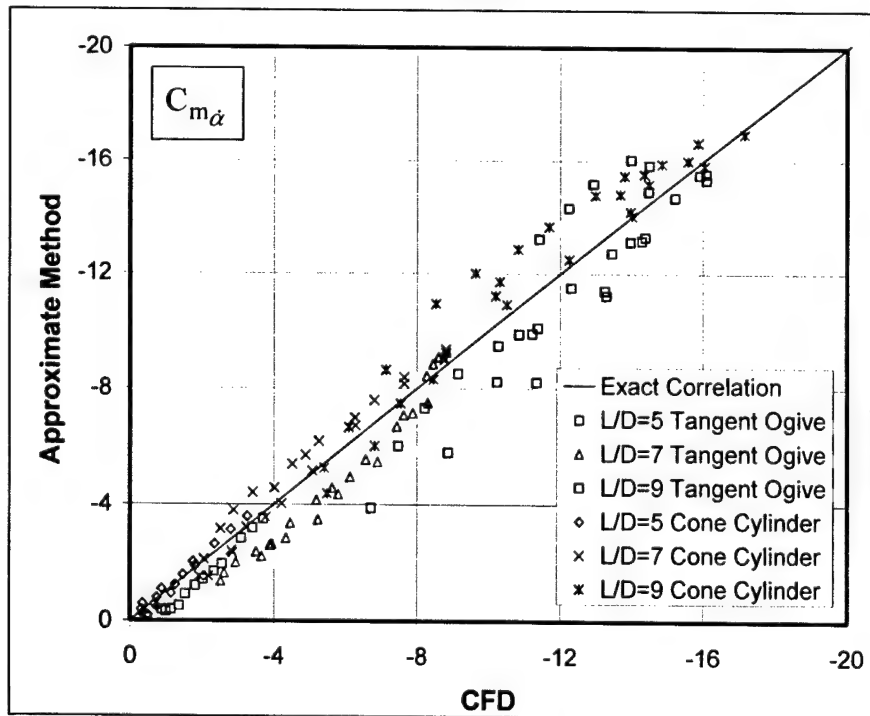


Figure 20. Correlation between approximate method predictions and CFD computations for $C_{m_{\dot{\alpha}}}$, cone cylinder and tangent ogive cylinder bodies, $L/D = 5, 7$, and 9 .

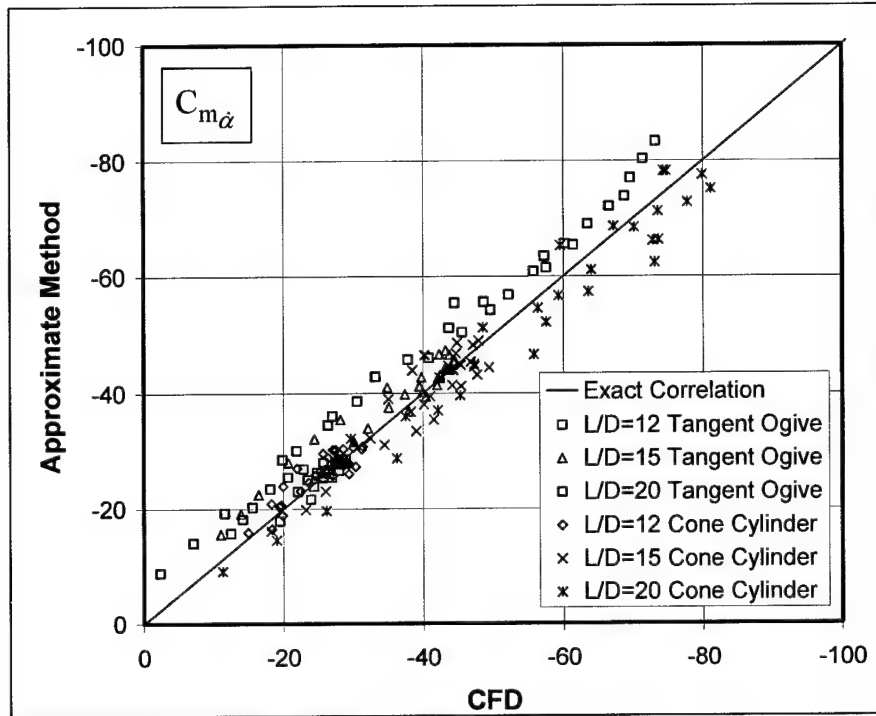


Figure 21. Correlation between approximate method predictions and CFD computations for $C_{m\dot{\alpha}}$, cone cylinder and tangent ogive cylinder bodies, $L/D = 12, 15$, and 20 .

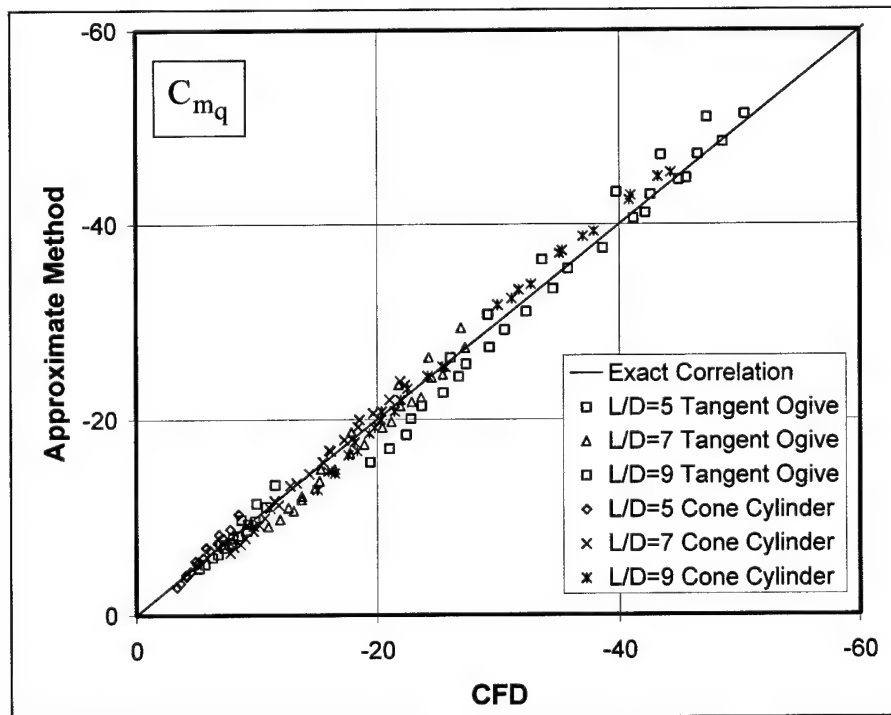


Figure 22. Correlation between approximate method predictions and CFD computations for C_{mq} , cone cylinder and tangent ogive cylinder bodies, $L/D = 5, 7$, and 9 .

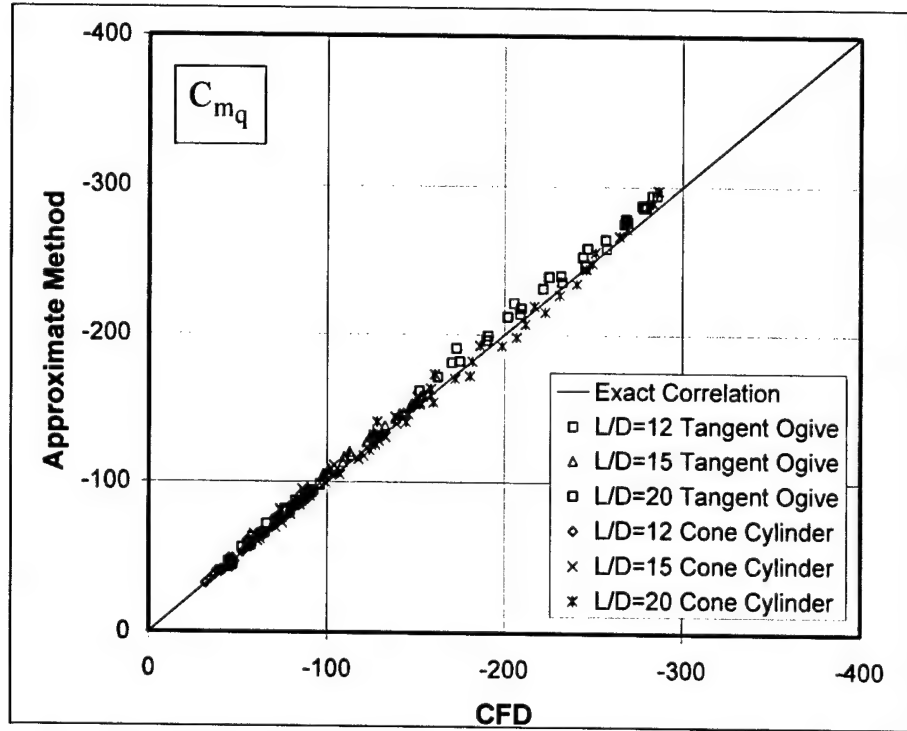


Figure 23. Correlation between approximate method predictions and CFD computations for C_{mq} , cone cylinder and tangent ogive cylinder bodies, $L/D = 12, 15$, and 20 .

$C_{N\dot{\alpha}}$ and $C_{m\dot{\alpha}}$. The variability shown in Figures 20 and 21 are a measure of the effectiveness of the correlation function $G(x)$. On the other hand, the reduced variability in Figures 22 and 23 indicates that relatively less error is obtained by applying equations 29 and 30. Most of the variability shown in Figures 22 and 23 results from the prediction of $C_{m\dot{\alpha}}$ which is one of the inputs used in equation 30. The additional terms in equations 29 and 30 appear to increase the magnitude of the coefficients without adding much additional error. An additional implication of these comparisons is that the variability of $C_{mq} + C_{m\dot{\alpha}}$ should be greater than C_{mq} but less than $C_{m\dot{\alpha}}$ since the sum is obtained by adding C_{mq} and $C_{m\dot{\alpha}}$.

The results presented in Figures 18 and 19 give a global assessment of the effectiveness of the approximate method. It is somewhat difficult from this data presentation to determine how well the model can be expected to perform when individual design variables are changed. Figures 24–27 show comparisons of the approximate method with CFD results for tangent ogive cylinder and cone cylinder bodies with a nose length of 2 calibers for Mach numbers between 2 and 5 and for body lengths of 5, 7, 9, 12, 15, and 20 calibers. The dominant effect shown in this set of figures is the increase in $C_{mq} + C_{m\dot{\alpha}}$ with increasing body length. A weaker variation in $C_{mq} + C_{m\dot{\alpha}}$ is observed with changing Mach number. The variation in the Mach number effect

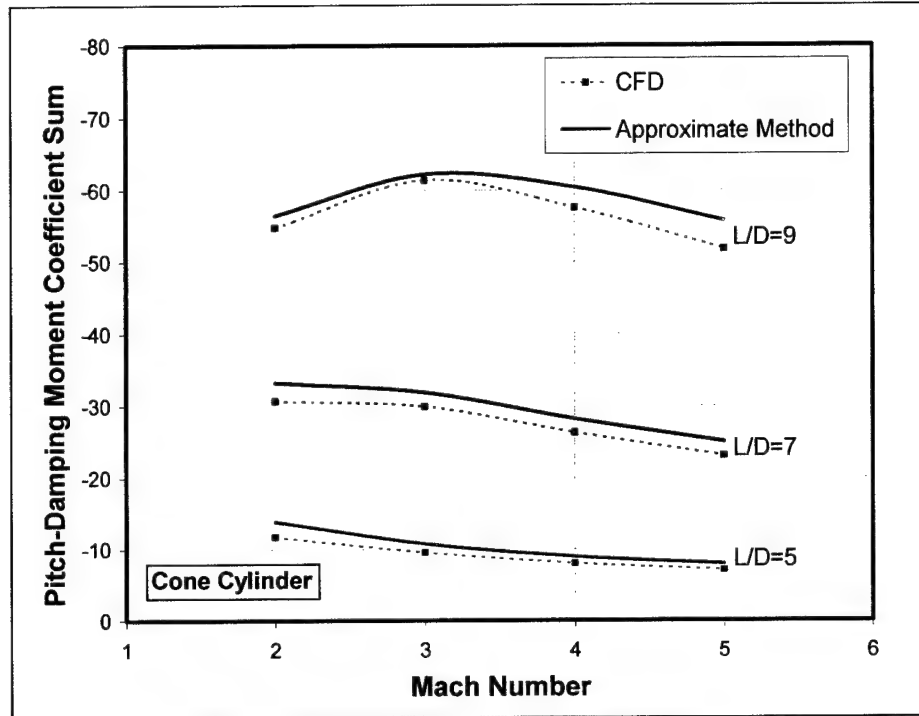


Figure 24. Comparison of predicted Mach number variation of $C_{m_q} + C_{m_{\dot{\alpha}}}$ obtained from approximate method and CFD computations, cone cylinder bodies, $L_{nose}/D = 2$, $L/D = 5, 7$, and 9 .

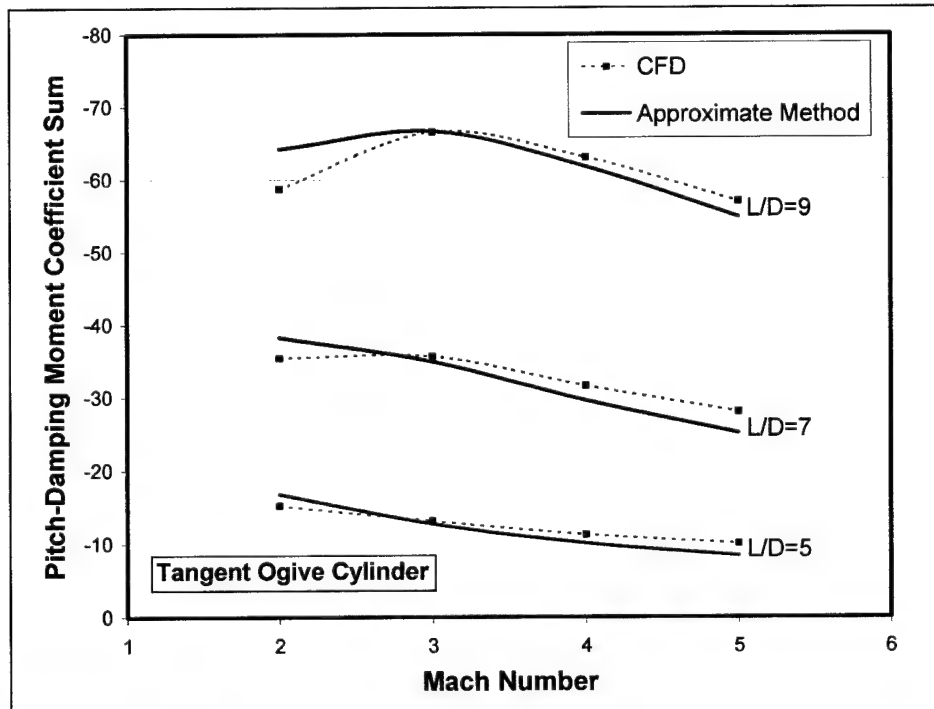


Figure 25. Comparison of predicted Mach number variation of $C_{m_q} + C_{m_{\dot{\alpha}}}$ obtained from approximate method and CFD computations, tangent ogive cylinder bodies, $L_{nose}/D = 2$, $L/D = 5, 7$, and 9 .

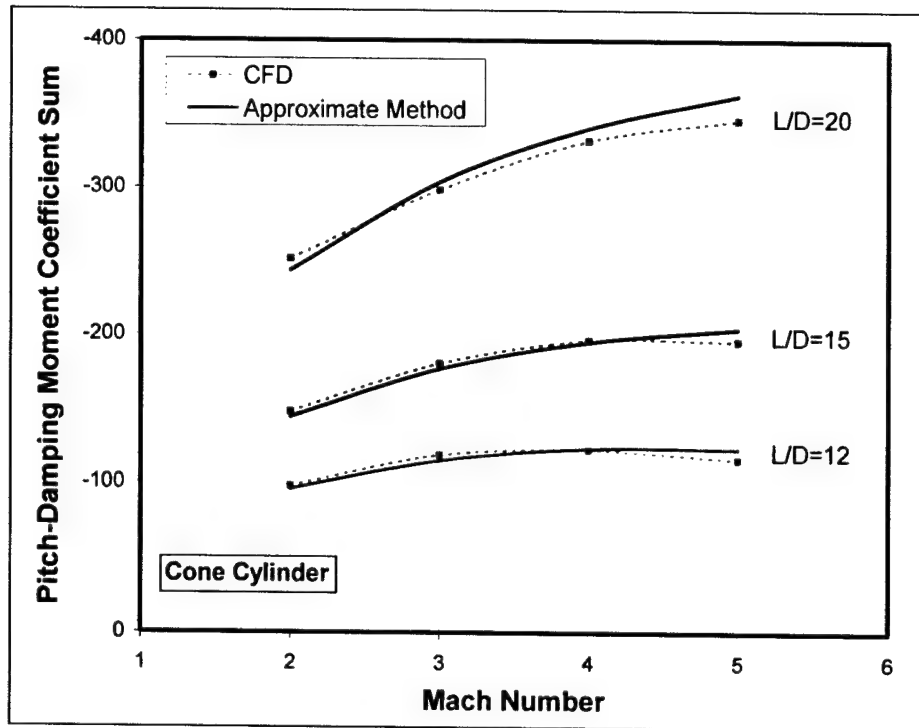


Figure 26. Comparison of predicted Mach number variation of $C_{mq} + C_{m\dot{\alpha}}$ obtained from approximate method and CFD computations, cone cylinder bodies, $L_{nose}/D = 2$, $L/D = 12, 15$, and 20 .

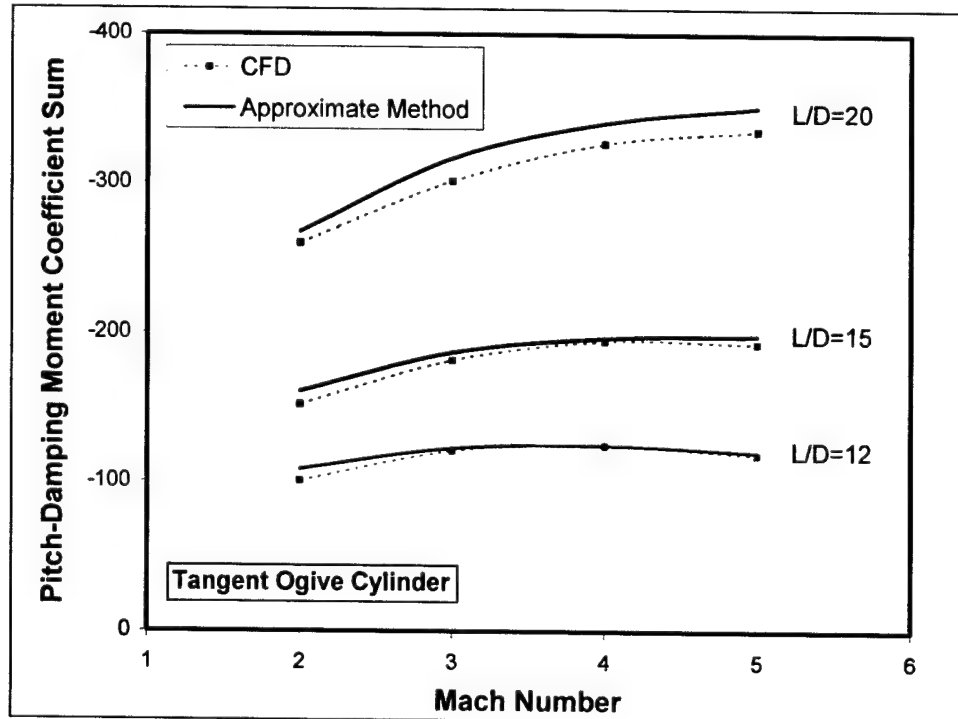


Figure 27. Comparison of predicted Mach number variation of $C_{mq} + C_{m\dot{\alpha}}$ obtained from approximate method and CFD computations, tangent ogive cylinder bodies, $L_{nose}/D = 2$, $L/D = 12, 15$, and 20 .

with increasing body length is well predicted by the approximate method compared with the CFD results. For the shorter body lengths, $C_{mq} + C_{m\dot{\alpha}}$ shows a decreasing trend with Mach number. However, as the body length increases this trend is reversed. For the nose and body lengths considered here, there is relatively little difference in the results between the two nose tips.

The effect of nose length on the predicted pitch-damping moment coefficient sum is shown in Figures 28 and 29 for an $L/D = 7$ body for both the tangent ogive cylinder and cone cylinder bodies. Both the approximate method and the CFD results show a similar decreasing trend of $C_{mq} + C_{m\dot{\alpha}}$ with increasing nose length. The approximate method also correctly predicts the relative differences between the conical and tangent ogive noses. Although some differences between the approximate method and the CFD results are apparent for the larger nose lengths, it should be noted that the 6-caliber nose is a rather extreme case because the cylindrical afterbody is only 1 caliber in length. Notwithstanding these differences, the approximate method appears to be capable of predicting the variation of $C_{mq} + C_{m\dot{\alpha}}$ with many of the design variables of interest.

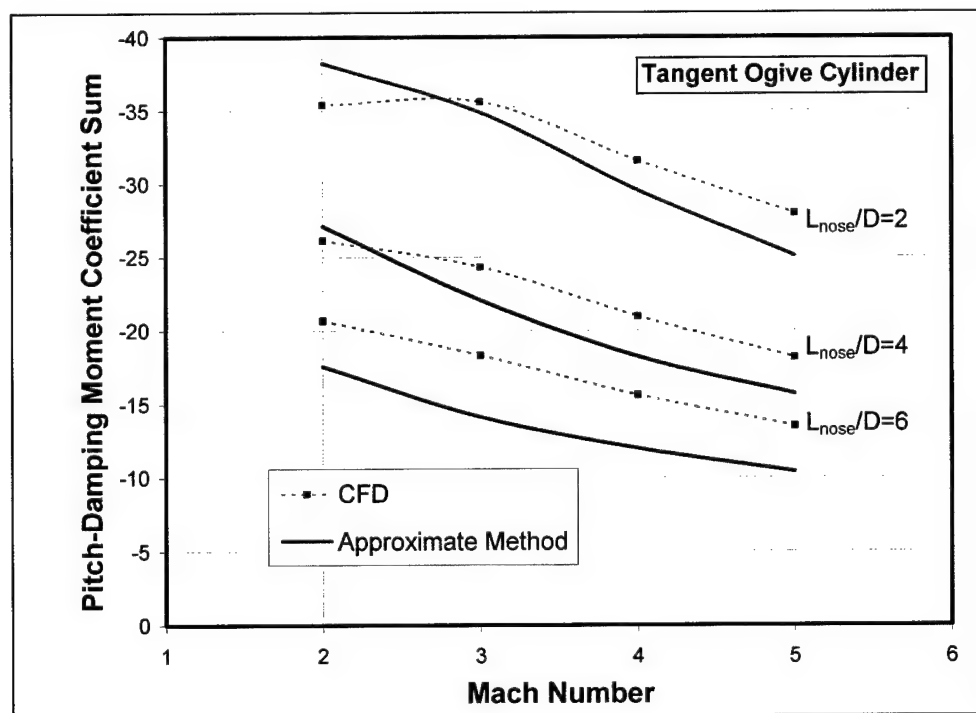


Figure 28. Comparison of predicted effect of nose length on $C_{mq} + C_{m\dot{\alpha}}$ obtained from approximate method and CFD computations, tangent ogive cylinder bodies, $L/D = 7$.

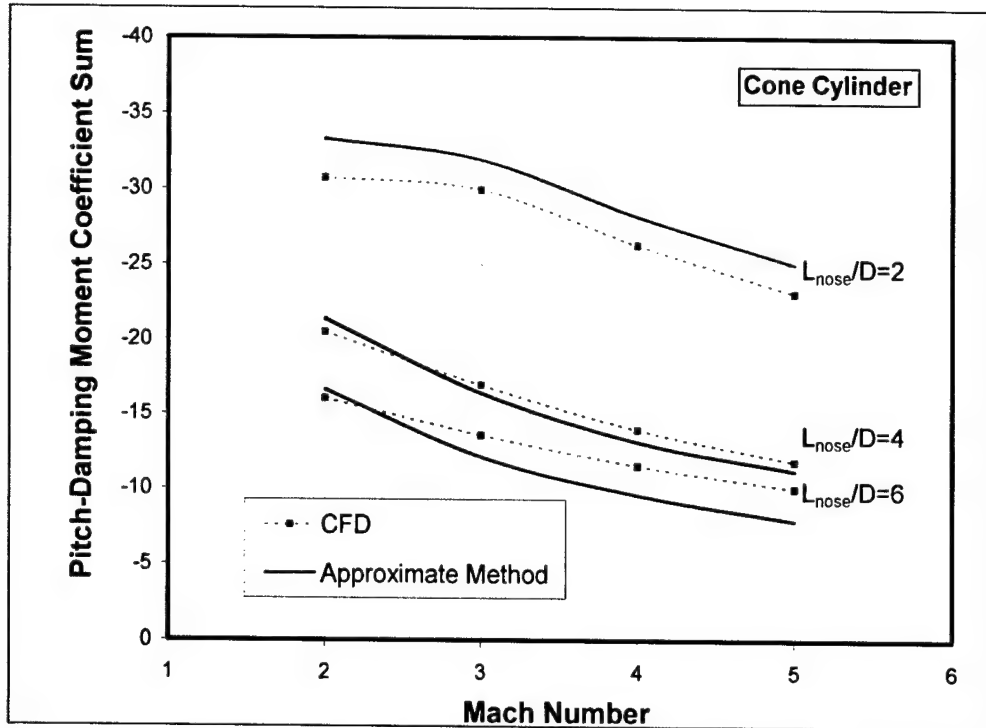


Figure 29. Comparison of predicted effect of nose length on $C_{mq} + C_{m\dot{\alpha}}$ obtained from approximate method and CFD computations, cone cylinder bodies, $L/D = 7$.

4. Conclusion

A semi-empirical method based on the slender body theory has been developed to predict the pitch-damping coefficients for axisymmetric projectile configurations. The method is based heavily on the slender body theory and some of the relationships between the aerodynamic coefficients that can be derived from the theory. Some slender body formulas are modified by the addition of correction factors that are derived from CFD predictions.

The CFD results allow a detailed investigation of the distribution of the pitch-damping force and moment along the body. The ability to accurately compute the distribution of these forces and moments provides information on how the body geometry (nose shape, carry-over region, center of gravity location, and overall length) produces the overall coefficients. Such an investigation would be very difficult to perform with experimental methods. The distribution also provides insight into reasons for the discrepancies observed in the slender body theory, which is an entirely local theory. Specifically, the slender body theory neglects the region immediately downstream of the nose (the carry-over region), which can be described with an integral that depends on upstream events. The validity of Sacks's relationship $C_{Nq} = C_{N\dot{\alpha}} - C_{m\dot{\alpha}}$ is demonstrated except at large L/D 's where a small correction is needed.

A modification to the slender body pitch damping theory is proposed in which the damping force coefficient $C_{N\dot{\alpha}}$ is related to the integral of the normal force coefficient slope, $C_{N\alpha}$. A new function, $G(x, M)$, is introduced to modify $C_{N\alpha}$ to accurately predict the damping coefficient.

CFD results are used to determine the factor G on the nose and cylindrical afterbody of an axisymmetric projectile in the supersonic velocity regime. Once $C_{N\dot{\alpha}}$ is determined, all the other damping force and moments can be directly calculated. One of the contributions achieved by basing $C_{N\dot{\alpha}}$ on $C_{N\alpha}$ and the factor G is to account for the carry-over of the nose normal force onto the cylinder. G is significantly affected by Mach number and an approximate transformation technique is shown to give acceptable results at supersonic speeds. In calculating the pitch damping coefficients, it is assumed that $C_{N\alpha}$ can be determined from an auxiliary method such as CFD or fast-design methods.

The technique has been applied to several axisymmetric projectile configurations. Comparisons have been made to the ANSR which is a family of secant ogive cylinder bodies of varying body length. Comparisons of the technique are made with both experimental and CFD data for this configuration to assess the accuracy of the method. To further assess the model, an extensive computational database was generated using CFD for a family of cone cylinder and tangent ogive cylinder bodies. Parametric variations of the body length (5–20 calibers), nose length (2–8 calibers) and Mach numbers (Mach 2–5) were performed to construct the database.

The model is simple and could be easily integrated into existing fast-design methods where its performance should be acceptable for preliminary design purposes. Extension of the modified slender body theory to bodies with fins or flares is currently being pursued.

5. References

1. Weinacht, P. Prediction of Pitch-Damping Aerodynamic Derivatives Using Navier-Stokes Computational Techniques. Ph.D. Dissertation, University of Delaware, Newark, DE, May 1996.
2. Weinacht, P.; Sturek, W. B.; Schiff, L. B. Navier-Stokes Predictions of Pitch-Damping for Axisymmetric Projectiles. *Journal of Spacecraft and Rockets* **1997**, 34 (6), 753–761.
3. Weinacht, P. Navier-Stokes Predictions of the Individual Components of the Pitch-Damping Sum. *Journal of Spacecraft and Rockets* **1998**, 35 (5), 598–605.
4. Weinacht, P. Prediction of Pitch-Damping of Projectiles at Low Supersonic and Transonic Velocities. American Institute of Aeronautics and Astronautics: Reston, VA, January 1998; AIAA Paper 97-0421.
5. Weinacht, P. Navier-Stokes Predictions of Pitch-Damping for a Family of Flared Projectiles. American Institute of Aeronautics and Astronautics: Reston, VA, September 1991; AIAA Paper 91-3339.
6. Weinacht, P.; Sturek, W. B. Navier-Stokes Predictions of Pitch-Damping of Finned Projectiles Using Steady Coning Motion. American Institute of Aeronautics and Astronautics: Reston, VA, August 1990; AIAA Paper 90-3088.
7. Moore, F. G.; McInville, R. M.; Hymer, T. *The 1998 Version of the NSWC Aeroprediction Code: Part I—Summary of New Theoretical Methodology*; NSWCDD/TR-98/1; Naval Surface Warfare Center: Dahlgren, VA, April 1998.
8. Vukelich, S. R.; Jenkins, J. E. Missile DATCOM: Aerodynamic Prediction on Conventional Missiles Using Component Build-Up Techniques. American Institute of Aeronautics and Astronautics: Reston, VA, January 1984; AIAA Paper 84-0388.
9. Whyte, R. E. *Spinner—A Computer Program for Predicting the Aerodynamic Coefficients of Spin Stabilized Projectiles*. Class 2 report no. 69APB3; General Electric Company: Burlington, VT, August 1969.
10. Moore, F. G.; McInville, R. M.; Robinson, D. I. *A Simplified Method for Predicting Aerodynamics of Multi-Fin Weapons*; NSWCDD/TR-99/19; Naval Surface Warfare Center: Dahlgren, VA, March 1999.
11. Moore, F. G.; Hymer, T. C. *The 2002 Version of the Aeroprediction Code: Part I—Summary of New Theoretical Methodology*; NSWCDD/TR-01/108; Naval Surface Warfare Center: Dahlgren, VA, March 2002.

12. Munk, M. *The Aerodynamic Forces on Airship Hulls*; NACA Report No. 184; National Advisory Committee for Aeronautics: Washington, DC, 1924.
13. Wood, R. M.; Murphy, C. H. Aerodynamic Derivatives for Both Steady and Nonsteady Motion of Slender Bodies. *Journal of the Aeronautical Sciences* **1955**, 22 (12), 870–871.
14. Bryson, A. E., Jr. Stability Derivatives for a Slender Missile With Application to a Wing-Body-Vertical-Tail Configuration. *Journal of the Aeronautical Sciences* **1953**, 20 (5), 297–308.
15. Nielsen, J. N. *Missile Aerodynamics*; McGraw-Hill: New York, 1960; Chapter 10, pp 363–371.
16. Sacks, A. H. *Aerodynamic Forces, Moments, and Stability Derivatives for Slender Bodies of General Cross Section*; NACA Technical Note 3283; National Advisory Committee for Aeronautics: Washington, DC, November 1954; p 27.
17. Weinacht, P.; Danberg, J. E. Evaluation of Sacks' Pitch-Damping Relationships. American Institute of Aeronautics and Astronautics: Reston, VA, August 2003; AIAA Paper 2003-5467.

List of Abbreviations

C_m	Pitching moment coefficient, $\frac{\bar{M}}{\frac{1}{2}\rho V^2 S_{\text{ref}} D}$
C_{m_α}	Pitching moment coefficient slope with respect to angle of attack, $\frac{\partial C_m}{\partial \alpha}$
C_{2m_α}	Static pitching second moment coefficient slope with respect to angle of attack
$C_{m_{\dot{\alpha}}}$	Pitch-damping moment coefficient slope, $\frac{\partial C_m}{\partial \left(\frac{\dot{\alpha} D}{V}\right)}$
C_{mq}	Pitch-damping moment coefficient slope, $\frac{\partial C_m}{\partial \left(\frac{q D}{V}\right)}$
$C_{mq} + C_{m_{\dot{\alpha}}}$	Pitch-damping moment coefficient sum
C_N	Normal force coefficient, $\frac{\bar{F}}{\frac{1}{2}\rho V^2 S_{\text{ref}}}$
C_{N_α}	Normal force coefficient slope with respect to angle of attack, $\frac{\partial C_N}{\partial \alpha}$
$C_{N_{\dot{\alpha}}}$	Pitch-damping force coefficient slope, $\frac{\partial C_N}{\partial \left(\frac{\dot{\alpha} D}{V}\right)}$
C_{Nq}	Pitch-damping force slope, $\frac{\partial C_N}{\partial \left(\frac{q D}{V}\right)}$
$C_{Nq} + C_{N_{\dot{\alpha}}}$	Pitch-damping force coefficient sum
\hat{D}	Local body diameter normalized by reference diameter
D	Reference diameter

\bar{F}	Force
$G(x)$	Correlation function used in computing $C_{N\dot{\alpha}}$
$H(x)$	Correlation function used in computing C_{Nq}
L/D	Body length-to-diameter ratio
L_{nose}/D	Nose length-to-reference diameter ratio
M	Mach number
\bar{M}	Moment
N	Number of data points used to compute overall root mean square (rms) deviation
q	Transverse angular rate of body
Re_r	Ratio of Reynolds number to baseline Reynolds number
S_{ref}	Reference area, $S_{\text{ref}} = \frac{\pi D^2}{4}$
V	Reference velocity
x	Axial coordinate normalized by reference diameter
x_{cg}	Axial location of center of gravity normalized by reference diameter
\bar{x}	Dummy variable of integration associated with axial coordinate x
X	Dimensional axial coordinate normalized by reference diameter
X_{cg}	Dimensional axial location of center of gravity normalized by reference diameter

Greek Symbols

α	Angle of attack
$\dot{\alpha}$	Angular rate associated with angle of attack
Δ	Individual error
ρ	Freestream density
σ	Overall root mean square deviation

INTENTIONALLY LEFT BLANK.